Part 1 – Impact of pyrolysis temperature and wood particle length on vapor cracking and char porous texture in relation to the tailoring of char properties

Przemyslaw Maziarka[1,2], Norbert Kienzl[3], Alba Dieguez-Alonso[4], Vanessa Fierro[5], Alain Celzard[5,6], Pablo J. Arauzo[2], Niklas Hedin[7], Wolter Prins[1], Andrés Anca-Couce[8], Joan J. Manyà[9], Frederik Ronsse[1]*

1 Department of Green Chemistry and Technology, Faculty of Bioscience Engineering, Ghent University, Coupure Links 653, 9000 Gent, Belgium

2 Department of Conversion Technology of Biobased Resources, University of Hohenheim, Garbenstraße 9, 70599 Stuttgart, Germany

3 BEST - Bioenergy and Sustainable Technologies GmbH, Inffeldgasse 21b, 8010 Graz, Austria

4 Laboratory of Transport Processes, Faculty of Biochemical and Chemical Engineering, TU Dortmund University, Emil-Figge-Str. 68, 44227 Dortmund, Germany

5 Université de Lorraine, CNRS, IJL, 88000 Épinal, France

6 Institut Universitaire de France (IUF), 75231 Paris, France

7 Department of Materials and Environmental Chemistry, Stockholm University, 10691 Stockholm, Sweden

8 Thermal and Fluids Engineering Department, Carlos III University of Madrid, Avda. de la Universidad 30, 28911 Madrid Leganés, Spain

9 Aragón Institute for Engineering Research (I3A), Thermochemical Processes Group, Escuela Politécnica Superior, University of Zaragoza, Crta. de Cuarte s/n, 22071 Huesca, Spain

KEYWORDS

Pyrolysis, Single particle, Bio-oil, Char, Pore size distribution

ABSTRACT

Pore size distribution is a key parameter in the performance of bio-based pyrolytic char in novel applications. In industrial-scale production, the size of feedstock particles typically exceeds a few millimeters. For such particle sizes, it is a challenge to tailor the final properties of the char based only on the process conditions (experimental and modeling-wise). Pyrolysis studies of single particles larger than a few mm provide datasets useful for modeling and optimization of the process. Part 1 of this research focused on the pyrolysis of single particles of beech wood, secondary cracking, and its effect on the char porous texture. It contains a quantitative assessment of the effects of five conversion temperatures (from 300 °C to 840 °C) and two particle dimensions (Ø8×10 mm and Ø8×16 mm) on the composition of the pyrolysis vapors and pore morphology of the char. Results from real-time temperature and mass changes are presented along with release profiles of 15 vapor constituents measured by infrared spectroscopy. Furthermore, characterization of the collected bio-oil (using GC-MS/FID) and the textural hierarchical structured char (through N_2 and CO_2 adsorption, Hg porosimetry, and SEM) was performed. Cracking of vapors above 500 °C was compound-specific. The polyaromatic hydrocarbons (PAHs) yield, between 680°C and 840 °C increased 5 times for 10 mm particles and 9 times for 16 mm ones. Besides the temperature, the PAH yield was suspected to correlate with particle length and PAHs/soot deposition in the micropores. Results showed that the macropores accounted for over 80% of the total pore volume regardless of the temperature and particle length. Increasing the particle length by 60% caused a reduction in the specific surface area (ca. 15% at 840 °C) of the resulting char, mainly due to a reduction in microporosity. Based on the findings, the production conditions for a specific char application are suggested. The obtained data will be used in a consecutive modeling Part 2 of this research, devoted to subsequent CFD modeling of the process.

1. Introduction

Bio-based pyrolytic chars are interesting for the adsorptive removal of pollutants and the production of electrodes.[1-3] They are recognized by the Intergovernmental Panel on Climate Change (IPCC) for soil application (biochar) to reduce greenhouse gas emissions.[4] However, there are limitations in the application of chars by uncertainties surrounding consistent properties.[5, 6] Although slow pyrolysis of biomass has been known since ancient times, a detailed understanding of certain processes during pyrolysis is limited, especially how the morphology of the char particles develops and how that should be quantified.[7] This translates to difficulties in the consistent production of biomass-derived chars for a given process with variability in the biomass. To improve this, more efforts need to be focused on the development of pyrolysis experiments and modeling to enhance the understanding of the chemical, physical, and morphological phenomena at the particle scale and its pores. The outcome may then be implemented in designs at the reactor level scale.[8]

Most laboratory studies on the slow pyrolysis of bio-based materials use wood, finely ground to a size of less than a few mm. Trunk (or stem) wood is usually preferred due to its low nitrogen, sulfur, alkali, and alkaline earth metal (AAEM) content, which allows for easier interpretation of the results.[9-14] Industrially, however, the size of wood particles used is typically significantly larger .[7] Wood reacts in the kinetic regime as a fine powder (size < ca. 1 mm, for T < 550 °C), but with larger particles, internal heat transfer becomes non-negligible, and the conversion moves into the thermally thick regime.[15-17] This regime is characterized by an inhomogeneous heating rate distribution.[18, 19] This in turn, leads to differences in the conversion route between specific points within a particle, which may have an impact on the overall structure development within a particle.

Studies of the pyrolysis of large wood particles (size > 1 mm) have often been limited to the effect of temperature and mass change along the conversion pathway.[14, 20-28] Nonetheless, some detailed single-particle studies also have been conducted. Gauthier et al. measured real-time changes in temperature and evolution of vapors during pyrolysis, and analyzed the composition of the collected condensable fraction, but did not report on the mass-loss profiles.[29] Anca-Couce et al. studied the temperature, mass loss, and release profiles of compounds during pyrolysis of wooden pellets without a change in particle size.[30] However, since the production of wood pellets requires milling and additives or binders, there is concern about inferring or extrapolating data from the pyrolysis of pellets to virgin wood. Lang et al. and Almuina-Villar et al. recorded the temperature, mass, and in-situ release of targeted species during pyrolysis of wooden particles, and assessed heterogeneous secondary reactions of primary volatiles, and the related formation of polyaromatic species and exothermicity in the process to intra-particle transport limitations.[14, 27]

The behavior of the vapors within the wood particle during pyrolysis affects the extent of pore development in the char. Studies indicate that the intensity of secondary reactions of vapors is directly related to the temperature and retention time of vapors in the reactor zone (even below 1 s).[31-35] In favorable conditions, vapors evolved in biomass pyrolysis can convert into PAHs and next into carbon/soot.[36, 37] When the phenomenon occurs intrinsically (within a particle), it may lead to solid deposition and affect the morphology of the pores. Most of the vapors from pyrolyzed wood particles are released through the particle surface at the end of the wood vessels/tracheids (longitudinal direction).[38, 39] Therefore, increasing the particle length affects the residence time of evolved vapors and, possibly, their secondary cracking at favorable temperatures. Westerhof et al. showed a significant relationship between particle length and yield of evolved vapors during pyrolysis of beech wood at 500 °C. However, in the study, the effect of particle length was created artificially, and the authors did not have high confidence in the effects observed.[40] Nonetheless, the correlation was proven in a study by Okekunle et al., who pyrolyzed single wood particles under non-isothermal conditions up to 700 °C.[41] Notably, previous studies focused on the relation between secondary cracking and retention time in the reactor zone and bio-oil yield as response variables.[34, 40] Therefore, the available information on the intrinsic occurrence of secondary reactions does not allow for quantification of its effect on the pore size distribution of the chars.

Since wood and its chars have pores over several length scales in the micro-meso-macropore range (conventionally measured from 0.35 nm to 500 μm), they can be treated as materials with a hierarchical structure. The properties of the chars derived from their pore size distribution (PSD) are attractive for several applications. For (electro)chemical applications, micro- and mesoporosity (0.35 nm – 2 nm and 2 nm – 50 nm, respectively) are required, and for soil applications, macroporosity (in the range of 0.1 μm – 500 μm) is a prerequisite. Information about how the micro- and mesoporosity of wood-derived char change with temperature can be found in the literature, but conclusive trends are not established yet.[5, 6] Recently, an analytical method has been suggested, which may help to obtain more consistent quantitative trends.[42] Despite the vast amount of data available in the literature on the macroporous PSD of virgin woods, there is little information regarding the changes in the macroporous PSD with conversion temperature.[43-49] Aside from two very recent studies based on micro-scale X-ray computed tomography (XCT), to the best of our knowledge, there are no previous single-particle studies reporting detailed investigations on the changes in pore morphology of chars.[50, 51] This makes the possibility of finding and quantifying the key factors that affect pore structure development extremely difficult. The aforementioned knowledge gaps generate uncertainty during modeling, since thermal conductivity and gas permeability (among other properties) depend on structural changes.[8] In the end, there is an inability to make reliable predictions based only on the process and feedstock parameters.

The first part of the research, referred to as Part 1, is related to the experimental assessment of single wood-based particle pyrolysis and data collection. It was structured to provide insights on the dependencies of the micro-, meso-, and macropore size distributions of chars with respect to the process parameters, as well as to provide a better understanding of the evolution of the char porous texture. A comprehensive experimental investigation of the conversion of a single beech wood particle is presented and covers: (1) the assessment of the effect of particle length for different pyrolysis temperatures on the composition of evolved products, with a focus on secondary cracking and related carbon deposition; and (2) the assessment of changes in bulk parameters (densities, shrinking) and detailed pore morphology (pore size distribution over micro-, meso-, and macroporosity domains) with the mentioned process parameters. Emphasis in the study was laid on quantitative assessment and data reliability and repeatability. It was made to ensure an appropriate foundation for consecutive parts of the research (Part 2) related to Computational Fluid Dynamic (CFD) modeling of single particle pyrolysis.

2. Materials and methods

2.1. Feedstock

European beech wood cylinders with diameter × length ($d \times l$) dimensions of 8 mm × 10 mm and 8 mm × 16 mm were provided by Rundstäb, Meyer & Weigand GmbH (Germany). The cylinders were cut in the longitudinal direction to align the cylinder's length dimension to the wood vessels/tracheids. All cylinders were drilled with a drill bit (d = 0.6 mm) to mount a thermocouple (d = 0.5 mm) into the geometrical center of the cylinder. Beech wood from the trunk was selected due to its low content in ash-forming elements, especially alkali and alkaline earth metals (AAEMs).[14, 28] Beech wood composition is presented in Table 1, with measurement details presented elsewhere.[52] The cylinders were dried overnight at 105 °C for moisture removal and thereafter kept in sealed glass vials to prevent subsequent moisture reabsorption.[18] For simplification, the cylinders were denoted by their length (i.e., "10 mm" and "16 mm").

Table 1. Bio-components content and elemental and inorganic composition of beech wood.

Parameter	Unit	Value (dry basis)
Cellulose	[wt.%]	40.0 ± 0.3
Hemicellulose	[wt.%]	34.1± 0.3
Lignin	[wt.%]	25.9 ± 0.5
C	[wt.%]	46.9 ± 0.3
H	[wt.%]	6.4 ± 0.1
N	[wt.%]	0.1 ± 0.0
O	[wt.%]	46.5 ± 0.3
K	[mg/kg]	921
Ca	[mg/kg]	891
Mg	[mg/kg]	315
all AAEM's	[mg/kg]	2127

2.2. Single-particle pyrolysis setup

The wood cylinders were pyrolyzed separately in a single-particle pyrolysis reactor located at BEST – Bioenergy and Sustainable Technologies GmbH (Austria). A scheme and validation of the reactor is presented by Sommersacher et al.[53, 54] An image of the device is given in Figure S1 (Supporting Information 1). The experimental procedure included single-particle pyrolysis trials for both lengths at five aimed temperatures of the particle (T_{aim}): 300 °C, 400 °C, 500 °C, 700 °C and 900 °C to investigate primary conversion of biocomponents and secondary reactions in the gas phase.[55] Online mass measurement was conducted by a balance (Mettler Toledo XS105DU), while the temperature at the center and surface of the particle was determined with two N-type thermocouples. Additional information on mounting thermocouples is provided in Section S1.3.

To avoid confusion between the aimed, applied, and obtained final temperatures, each conversion scenario investigated in this study will be denoted as TX_YY, where TX represents the temperatures for the scenario and YY indicates particle length, e.g., T1_10 represents the scenario where: T_{aim} = 300 °C and using a 10 mm particle with corresponding final temperatures of reactor wall (T_W), flue gas (T_G) after the reactor and gas dilution (applied to hinder secondary reactions of vapors after the particle) and center (T_C) and surface (T_S) of the particle. A summary of the conversion parameters for each scenario is presented in Table 2.

Table 2. Temperatures and gas flows during pyrolysis of a single cylindrical particle of beech wood (l – particle length, T – temperature, $\dot{V}$ – volumetric flow rate, t – time and subscripts aim – aimed value, W – reactor wall, G – flowing gas, B – reactor bottom, D – diluter and c – conversion).

Scenario [-]	l [mm]	T_{aim} [°C]	T_W [°C]	T_G [°C]	$\dot{V}_B$ [Nm^3/min]	$\dot{V}_D$ [Nm^3/min]	t_c [min]
T1_10	10	300	353 ± 13	330 ± 7	10	_	15
T2_10		400	475 ± 6	404 ± 4	10	_	10
T3_10		500	570 ± 3	485 ± 5	10	_	10
T4_10		700	820 ± 1	485 ± 4	10	10	10
T5_10		900	1050 ± 1	508 ± 4	10	10	5
T1_16	16	300	360 ± 16	367 ± 4	10	_	15
T2_16		400	475 ± 6	404 ± 3	10	_	10
T3_16		500	569 ± 2	406 ± 6	10	_	10
T4_16		700	820 ± 1	490 ± 3	10	10	10
T5_16		900	1050 ± 1	534 ± 3	10	10	5

The inlet temperature of the N_2 (99.99 vol. %) was 20 – 30 °C. The reactor was initially heated to the requested wall temperature (T_W), which was chosen to be slightly higher than T_{aim}. Such an approach was chosen to compensate for heat dissipation and the cooling effect of the flowing gas, which was important, especially at higher temperatures. The inert gas was supplied to the reactor only from its bottom when $T_{aim} \leq 500$ °C. For scenarios where $T_{aim} > 500$ °C, the inert gas was provided from the bottom of the reactor and through a porous tube diluter, coupled to the flue gas outlet. The sample, located on the balance and equipped with thermocouples, was initially inserted into the reactor with a thermal protective cooling jacket to prevent premature sample decomposition and keep it at a temperature of ca. 20 – 30 °C. The conversion time (t_c) and the recording of the online measurement data (temperatures, mass, release of vapors) were controlled corresponding to the time of removing and placing the cooling jacket back again. The mass and temperature recording started immediately after the insertion of the sample into the reactor. The measurement of the released volatiles started after the removal of the cooling jacket. The offset between both measurements was ca. 10 s. This time was required to check if the reactor was sealed correctly (no oxygen detected), if the balance worked appropriately, and to synchronize the start of the FT-IR measurements with the removal of the cooling jacket. The conversion time required to obtain a constant mass (less than 1 % variation in relative terms for more than 10 s) varied among the aimed temperatures. When the cooling jacket was placed back, a high flow of N_2 was applied to quench the sample to room temperature and stop its further conversion. Finally, the sample was removed from the reactor, dismounted from the thermocouples, removed from the balance, and placed in a sealed glass vial.

Recording of the vapor release profile and collection of bio-oil was made in triplicate for all investigated scenarios. However, some measurements had to be repeated due to experimental outliers (elevated moisture content, sample oxidation, or incorrect mass loss measurement). Details are provided in Section S1.2. The char was collected in one piece to allow for consecutive measurements of geometrical changes and mercury porosimetry. Therefore, additional replicates had to be made when a char sample split (or exploded, in some cases). A video of an explosion of a cylindrical particle is presented in Supporting Information 2.

2.3. Analysis of released vapors and collection of bio-oil

The real-time release of vapors during pyrolysis was monitored with a FT-IR analyzer (Ansyco Gasmet DX 4000). Details about the calibration of the FT-IR can be found in the work of Anca-Couce et al.[30] The measurement included 15 evolved volatiles: CO_2 (carbon dioxide), CO (carbon monoxide), CH_4 (methane), C_2H_4 (ethene), C_2H_2 (acetylene), C_3H_8 (propane), C_3H_6 (propene), HCHO (formaldehyde), CH_3CHO (acetaldehyde), CH_3COOH (acetic acid), C_2H_5COOH (propanoic acid), CH_3OH (methanol), C_2H_5OH (ethanol), $C_5H_4O_2$ (furfural) and H_2O (water). Additionally, compounds with similar characteristics were grouped, where light hydrocarbons (LH) included C_2H_4, C_2H_2, C_3H_8, and C_3H_6; and light condensables (LCS) included HCHO, CH_3CHO, CH_3COOH, C_2H_5COOH, CH_3OH, and C_2H_5OH. The mass yield was obtained as a time integral of the release profile (sum of released masses). The yield per initial biomass was obtained by dividing the mass of vapor/gas by the initial mass of the wood particle. The data recording was started manually and simultaneously with the removal of the cooling jacket, and it lasted until the jacket was put on back again (t_c). The device recorded the spectra with an approximate interval of ca. 1 s. Releases of CO_2 and CO were analyzed simultaneously with a flue gas analyzer (ABB EL3020), based on nondispersive infrared spectroscopy (NDIR), to validate the release profiles and yields obtained from FT-IR for these two gas species. Both analyzers were assessing the flow of the vapor/gas compounds on a volumetric basis ((m^3/m^3)/s), which was further re-calculated into concentration on a mass base (kg/s). Detailed information about the smoothing, recalculation, and averaging can be found in Section S1.2. The comparison between the release profiles and yields obtained with FT-IR and NDIR is provided in Section S2.1.

For bio-oil collection, the reactor outlet was connected to a tar collection setup based on the CEN/TS 15439 tar protocol. An image of the bio-oil collection setup used for this purpose is provided in Figure S2. In brief, the device was equipped with scrubbers organized in sequence. Each scrubber was filled with 80 mL of isopropanol cooled by an external cooling circuit to a temperature of -20 °C. The flow through the scrubbers was induced by a pump connected to the outlet of the last scrubber. The under-pressure generated by the pump was adjusted to match the set flow (Table 2). For $T_{aim} \leq 500$ °C, only two scrubbers were filled with isopropanol. For $T_{aim} > 500$ °C, an additional scrubber was added (3 scrubbers in total) to ensure complete condensation of the vapors. The liquids obtained (isopropanol with dissolved bio-oil and water) were stored in polypropylene vials (50 mL) at room temperature on the assumption that the significant dilution of bio-oils should prevent further reactions (e.g., re-polymerization) during storage.

2.4. Bio-oil analysis with GC-MS/FID

Details of the procedure used to prepare the liquid samples, the GC-MS/FID measurement procedure applied, and the compounds identified can be found in Section S3. The liquid samples initially collected (bio-oil dissolved in isopropanol) were too low in concentration to be analyzed, so their bio-oil concentration had to be increased. Therefore, samples from 3 replicates of each scenario were pooled and evaporated at 45 °C and 100 mbar in a rotary evaporator (Heidolph Instruments, Hei-VAP) and consecutively dissolved in 4 mL of acetonitrile.

The liquid sample was injected by an automatic sampler into the gas chromatograph (GC) (Thermo Fisher Scientific Trace GC Ultra). The GC oven was equipped with a Restek RTX-1701 capillary GC column (60 m × 0.25 mm × 0.25 μm), and helium (≥ 99.99 vol. %) was used as the carrier gas. The output of the GC column was connected to a single quadrupole mass spectrometer (MS) with electron ionization (Thermo ISQ MS) for qualitative assessment and a flame ionization detector (FID) for quantitative assessment. Compounds were identified manually, based on their retention times and fragmentation patterns (NIST database) and in relation to literature sources.[29, 56-60] Each compound identified with GC-MS/FID (n > 90) was assigned to one of the specific groups related to its chemical structure: AOX – aliphatic oxygenated compounds (linear compounds with oxygen), COX – cyclic oxygenated compounds (cyclic compounds with oxygen not incorporated into a ring), FU – furanic compounds (heterocyclic compounds with oxygen incorporated into a ring), PH – phenolic compounds (phenol and its derivatives) and PAH – polyaromatic hydrocarbons (compounds with more than one benzene ring).

The calibration of the FID was made with 5 compounds: acetic acid, furfural, phenol, guaiacol, and naphthalene, which were considered as representative compounds for the obtained bio-oils according to the classification provided above. Since the number of identified compounds was much higher than that of calibrated compounds, their concentration was calculated using the Effective Carbon Number method (ECN). In the literature various newly developed methods for ECN calculation can be found, but in this study, the method presented by Scanlon and Willis was applied since its use was validated in other studies.[60-63]

2.5. Dimensional changes

The particle dimensions were measured using a digital micrometer with a spherical anvil (Hogetex IP54, from 0 mm to 25 mm, ± 0.004 mm). The obtained chars had the shape of elliptic cylinders. Therefore, their dimensions in the longitudinal, radial, and tangential directions were measured. The dimensional changes of the particles are based on average values from several measurements ($n \geq 2$). Measurement details are presented in Section S5.1.

2.6. Helium pycnometry

Prior to helium pycnometry, the solid samples were ground in an agate mortar to reduce any intraparticle diffusion limitation in the subsequent measurements.[64, 65] For char, samples from at least two replicates were ground and homogenized to provide enough material for analysis. Helium pycnometry measurement was conducted using an AccuPyc 1330 pycnometer (Micromeritics Instrument Corporation).

2.6. Gas adsorption with N_2 and CO_2

Gas adsorption isotherms were acquired using a Nova 4000e gas adsorption analyzer (Quantachrome Instruments). Sample degassing was performed at 180 °C (for at least 24 h). N_2 adsorption data were recorded at –196 °C, at relative pressures from 10^{-3} to 0.99. CO_2 adsorption data were recorded at 0 °C, at relative pressures of 5×10^{-5} to 10^{-3}. Adsorption isotherms were presented in a previous study.[52] Pore size distributions (PSDs) were calculated using the SAIEUS software (v. 3.2), which shows good reliability for the assessment of porous carbon materials.[42, 66-69] Further details on the calculation method can be found in Section S5.2.

2.7. Mercury intrusion porosimetry (MIP)

Mercury intrusion porosimetry (MIP) measurement was conducted on whole char particles using an AutoPore IV 9500 mercury porosimeter (Micromeritics Instrument Corporation). Prior to intrusion, the sample was evacuated to 10.67 Pa for 5 min. Applied pressure started at 0.0036 MPa and ended at 414 MPa. Particle bulk density was assessed at the pressure of 0.0036 MPa. Pore diameter at a specific pressure was calculated using the Washburn equation with contact angle correction for carbonaceous materials. Further details regarding MIP data processing and PSD of each replication are available in Section S5.3. and Section S5.4.

2.8. Assessment of hierarchical porous structure (micro-meso-macro)

The full PSD (0.35 nm – 500 μm) was analyzed to assess the porosity of the resulting chars, which exhibited a hierarchical structure. The full PSD was obtained using CO_2 adsorption data (0.35 nm – 1.5 nm), N_2 adsorption data (1.5 nm – 20 nm), and MIP data (20 nm – 500 μm). The merging of the PSDs from CO_2 and N_2 was calculated according to the work of Maziarka et al.[42] The starting point of PSD obtained with MIP was selected at 20 nm. This choice was made because of concerns about the reliability of evaluating smaller pores with MIP (e.g., deformation of the material at high pressure).[70]

Two classifications of pores available in the literature are not fully compatible, and, to some extent, neither is suitable for evaluating materials with a hierarchical structure (micro-meso-macropore classification). One classification, established by the International Union of Pure and Applied Chemistry (IUPAC), is devoted to materials whose application is related to their specific surface area (SSA), such as adsorbents and catalysts.[71] The other, established by the Soil Science Society of America (SSSA), is devoted to materials whose application is related to pore volume (V_{pore}) such as soils and their components.[72] The proposed new classification, based on a combination of the IUPAC and SSSA classification, is presented in Table 3. On its basis, the SSA and V_{pore} for specific pore groups have been obtained. As in SSSA classification, pores larger than 500 μm (0.5 mm) are not treated as structural pores, and pores above that size have, therefore, been excluded.

Table 3. Classification of pore size ranges for hierarchically structured materials (e.g., chars derived from pyrolytic biomass) with comparison to IUPAC and SSSA classifications.

IUPAC	SSSA	This study	Abv.	Range
Ultra micropores	Cryptopores	Small micropores	Mi-S	0.35 nm – 0.7 nm
Micropores	Cryptopores	Large micropores	Mi-L	0.7 nm – 2 nm
Mesopores	Cryptopores	Small mesopores	Me-S	2 nm – 50 nm
Macropores	Cryptopores	Large mesopores	Me-L	50 nm – 100 nm
Macropores	Ultra micropores	Ultra small macropores	Ma-U	0.1 μm – 5 μm
Macropores	Micropores	Small macropores	Ma-S	5 μm – 30 μm
Macropores	Mesopores	Medium macropores	Ma-M	30 μm – 75 μm
Macropores	Macropores	Large macropores	Ma-L	75 μm – 500 μm

2.9. Scanning electron microscopy (SEM).

Scanning electron microscopy (SEM) images were taken to assess the morphology of the char solid structure. Analysis was performed using a JSM-7000 (JEOL) microscope. The char samples were ground beforehand in an agate mortar, and the powdered material thus obtained was placed on the stud coated with double-sided adhesive tape.

3. Results

3.1. Temperatures and mass change profiles

Averages (n ≥ 2) of the surface (T_S) and center (T_C) temperatures of the particle, as well as the char mass yields (Y_M) for all investigated scenarios are presented in Table 4. It was noted that the final temperatures and solid yields were quite similar. T_C depends on the gas temperature, reactor temperature, gas flow rate, and radiative heat transfer at temperatures above 500 °C – 600 °C. The latter explains the differences between the aimed and measured temperatures at higher temperatures. The precise calibration of the conversion conditions to match the aimed temperature was not conducted since the obtained final particle center temperature was within the desired range to observe the investigated phenomena. Deviations in T_C, T_S and Y_M were most noticeable for scenarios T1 and T3 between particles of different lengths. Especially for scenario T1, T_C and T_S were higher by ca. 10 °C for the 16 mm cylinder (in comparison to the values recorded for the 10 mm particle). This may explain the lower Y_M by ca. 5 wt.% in scenario T1_16. The cause of such deviation was a ca. 30 °C higher temperature of the carrier gas (see Table 2). In scenarios T3, T_G was higher by ca. 70 °C in T3_10 than in T3_16, which also translated to a lower Y_M in the latter scenario. While in scenario T1, the effect of T_G was distinguishable in the T_S value, for scenario T3, it showed a negligible effect. In scenario T5, the reactor conditions and final temperatures were similar, while Y_M was distinguishably higher for scenario T5_16 (by ca. 2 wt.%). It was suspected that the secondary vapor reactions were more profound in the longer particle, i.e. in scenario T5_16 compared to T5_10 and led to the observed effect on the char yield. Overall, despite a deviation in T_G between scenarios, it did not have a drastic effect on T_C, T_S and Y_M. Therefore, the obtained results are considered reliable, but further analysis should consider the implications of deviations in the process conditions. The typical temperature-related trend of the reduction in char yield and increased yield of released vapors observed in this study is also well-explained in the literature.[73-77]

Table 4. Comparison between the averaged (n ≥ 2) temperatures at the particle surface (T_S) and in the center (T_C) and char yield (Y_M) for all investigated scenarios.

Scenario [-]	l [mm]	T_{aim} [°C]	T_S [°C]	T_C [°C]	Y_M [wt.%]
T1_10	10	300	307 ± 5	305 ± 5	66.7 ± 0.1
T2_10		400	412 ± 1	404 ± 1	26.8 ± 0.1
T3_10		500	485 ± 1	488 ± 1	16.6 ± 1.0
T4_10		700	691 ± 9	677 ± 9	13.3 ± 0.4
T5_10		900	868 ± 6	839 ± 8	10.7 ± 0.2
T1_16	16	300	322 ± 3	317 ± 1	62.0 ± 2.6
T2_16		400	414 ± 1	405 ± 1	25.7 ± 0.4
T3_16		500	488 ± 1	479 ± 3	20.0 ± 0.1
T4_16		700	702 ± 4	681 ± 4	12.9 ± 0.7
T5_16		900	872 ± 4	829 ± 1	12.0 ± 0.8

Time-dependent curves of the average (n ≥ 2) temperatures and mass are shown in Figure 1 for the studied particle lengths and pyrolysis temperatures. The differences in the temperature of the surface and center of the particle are a signature of a thermal driving force in the radial/tangential direction with a colder center. The origin of the specific shape of the center temperature profile and the overall exothermicity of the pyrolytic conversion process have been discussed in the literature.[18, 73, 78] Therefore, since both those subjects are not the main aim of this work, an in-depth discussion on this matter will be omitted. Nevertheless, in Figure 1, for scenarios T2_10 and T3_10, a peak in the temperature evolution at the particle center temperature can be noticed (around 120 – 130 s), where the center temperature also exceeds the surface temperature, as is shown for scenarios T2_10 and T3_10 in Figure 1. A similar peak can also be observed in other pyrolysis studies of single particles, as well as at reactor -scale pyrolysis, mostly around 500 °C.[21, 22, 30, 55, 79-81] The literature indicates that the main reason for this peak formation is related to exothermic heat generation due to condensation reactions of the carbon structures.[18, 81-83] The difference in the rate of heat production is presumed to be the cause for a less pronounced exothermic peak in scenarios T2_16 and T3_16 in comparison to scenarios T2_10 and T3_10, respecitively. Regardless of the occurrence, the presence of this peak can be hidden when the rate of heat production becomes lower than the heat influx from the particle's exterior to the volume in the vicinity of the center of the particle. When the conversion temperature exceeds 500 °C, the magnitude of the heat influx to the center of the particle increases (i.e., the radiative component starts to impact the heat transfer). Then, the thermal effects (i.e. exothermicity) of the condensation reactions are insufficient to induce a visible peak of the temperature at the center of the particle.[18] Therefore, for scenarios T4 and T5, this peak was no longer noticeable (c.f. Figure 1).

As it can be seen in Table 4, the final temperature of the surface exceeded the temperature of the particle center for scenario T3_10. Nonetheless, the excess was in the range of 2 °C, so relatively low. It is suspected that the main reason for the occurrence of a higher final temperature at the particle's center compared to its surface was related to an imperfection in the temperature measurement by the applied thermocouple mounting. It cannot be ruled out that, due to the shrinkage of the particle, the thermocouple located on the particle surface detached from the surface and started to show the temperature of the gas phase in the vicinity of the particle. More details on the subject are provided in Section S1.3.

As pointed out in Section 2.1., particles were dried to a moisture-free state prior to conversion. Therefore, the replicates that indicated re-absorption of moisture from the environment were excluded from the dataset (or repeated, if necessary). The possible source of moisture in the sample was related to improper sealing of the storage vial or a too long time between opening the sample vial and insertion of the sample into the reactor. Therefore, the results presented in Table 4, as well as in Figure 1, are results from the successful conversion of moisture-free particles. As it can be observed in Figure 1, the conversion of the sample did not start immediately at the beginning of the plot (0 s). The reason is related to the applied time offset for the measurements (see Section 2.2). More details on the exclusion of results from replicates contaminated with moisture and the measurement time offset are additionally provided in Section S1.3.

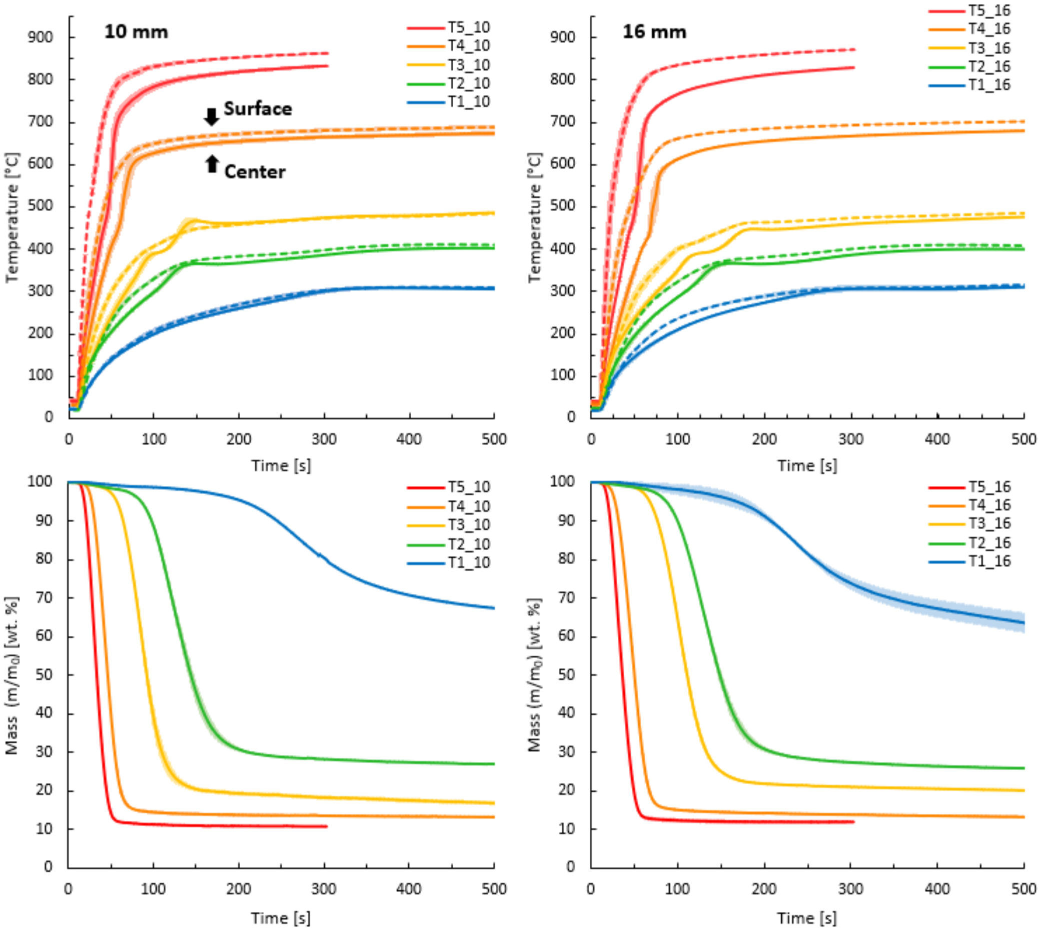

Figure 1. Averaged (n ≥ 2) temperature profiles (top: solid line – center, dashed line – surface) and mass profiles (bottom) for all investigated scenarios (faded band - standard deviation).

Additional averaged profiles of differential temperature for all scenarios are presented in Figure S7. Unfortunately, a global value of the Biot number cannot be provided for the investigated scenarios due to the high complexity of the investigated material. The main reasons are the transient (conversion and temperature) and anisotropic character of thermal conductivity and of the characteristic length of the particle. Nonetheless, a rough estimation is provided to indicate a range of Biot numbers encountered in this study. The external convective heat transfer coefficient for the Ø8 mm cylinder, calculated according to Churchill–Bernstein equation, was ca. 20 and 30 $W/(m^2 \cdot K)$ for conversion temperatures of 300 °C and 840 °C, respectively.[84, 85] The thermal conductivity of wood and char in the radial direction were sourced from the work of Lee et al.[86] The estimation with applied assumptions suggests that in the investigated cases, the Biot number (radial direction) for wood should be within a range from 1.5 to 2.5 and for char within a range from 2.0 to 3.5. The estimated ranges are in agreement with values found in literature. For cases where the Biot number is higher than 0.1, the internal thermal conduction is the limiting factor of heat transfer, in opposition to heat delivered to the particle by external convection.[16, 55] The estimated Biot number ranges indicate that for all investigated scenarios, temperature gradients were not negligible inside the particle during conversion, which also can be noticed in Figure S7. Additionally, the literature indicates that a non-negligible gradient of heating rate can be expected during single particle conversion, which is directly related to the conversion temperature.[18] Therefore, a similar situation was expected for the investigated samples. For a conversion temperature of ca. 300 °C, the heating rate gradient was assumed to be negligible due to a high similarity between the center and surface temperature profile (cf. Figure 1) and relatively low difference between them (e.g., ca. 25 °C for 16 mm particle, Figure S7). For a conversion temperature of ca. 480 °C, the gradient of heating rate increased, and its effect became noticeable when the temperature at the center of the particle exceeded ca. 200 °C. For scenarios T2 and T3, the thermal effects of the bio-polymer conversion were assumed to be the main factor that caused the deviation in the heating rate distribution. For scenarios T4 and T5, the conversion temperature exceeded 500 °C. For those scenarios, the deviation between the temperature profiles was well pronounced, which resulted in a noticeable difference in temperatures, especially in the initial times of the conversion (above 100 °C in the first 50 s, Figure S7). Therefore, the results from scenarios T4 and T5 indicated the presence of a heating rate gradient within the particle. Additionally, such results indicated that for scenarios T4 and T5, the conversion occurred in a layered way, whereas in the outer layer (volume close to the surface), the conversion occurred with a much higher heating rate than in the internal volume. Particle conversion in a layered way may affect yields, which needs to be taken into account in further discussion.[18]

To conclude, the results obtained were consistent and the standard deviation from averaged replicates was very low (cf. Table 4). Apart from the scenarios T1_10 and T1_16, the 10 mm sample reached the target temperature slightly faster in all other cases, leading to a faster mass loss. In Figure 1, a difference in time location and extent of the exothermic peak can be observed between scenarios T3_10 and T3_16. However, for scenarios T2_10 and T2_16, this difference was marginal. Therefore, it is likely that for the T3_10 and T3_16 scenarios, the discrepancy is caused by slight differences in reaction conditions (cf. Table 2). Additionally, it can be pointed out that since the 10 mm particle converts faster, the exothermic effect at its center could occur with a higher rate, leading to a higher temperature peak than in scenario T3_16.

3.2. Release of volatiles and their yields

The effects of temperature and particle length on the component-specific yields are shown in Figure 2. The observed dependencies were highly repeatable. Over the range of investigated temperatures, it can be observed that the concentration of CO_2 in the outflow gas was higher than that of CO only up to T_C = ca. 480 °C. Above that temperature, the share of CO rose, and at the final temperature, ca. 840 °C, the pyrolysis gas contained more CO than CO_2, which is consistent with the literature. This trend is related to the formation of CO in secondary reactions of volatiles (cracking).[58, 77] The yield of LCS and furfural increased gradually up to 480 °C, and a further increase in temperature led to their significant yield reduction. For LCS, the temperature at which this reduction occurred was between 680 °C and 840 °C, while for furfural, it was between 480 °C and 680 °C. The drop in yield can be attributed to the secondary cracking reactions of compounds included in LCS and furfural and a clear difference in thermal stability towards the cracking reaction between both groups of compounds. For conversion temperatures up to ca. 500 °C, higher CO_2 and lower CH_4 and LCS yields were observed for shorter particles. Then, with the temperature increase, the difference in yields between both particle lengths became inconclusive, but noticeable. The particle length could have affected the extent of primary degradation of the bio-components ascribed to differences in the heating rate or evaporation of evolved anhydrosugars.[87, 88] However, the evaporation effect is inconsistent with the higher yields of CO_2 and H_2O observed for the longer particle. The increase in H_2O yield with temperature did not show the same steep rising trend as for CO or CH_4. It is suspected that the Boudouard reaction could be an enhancing factor for the rise in the CO yield, especially at 840 °C (indicated also by a slight drop in CO_2 yield).[89-92] Between 680 °C and 840 °C, a drop in the H_2O yield for both particles can be observed. H_2O is mainly formed in primary degradation processes.[16] The yield reduction is expected to be related to steam gasification of char, which becomes relevant above 600 °C, but is more effective at higher temperatures.[18] An additional factor of water yield reduction could be attributed to water gas shift and/or steam cracking of evolved vapors, since the process occurs in temperatures above 800 °C. The origin of specific compounds in pyrolytic vapors from initial bio-components, as well as their secondary decomposition, has already been extensively discussed in the literature.[16, 58, 77, 93-95] Therefore, this work will not elaborate further on this subject.

The average mass yields of specific compounds measured with FT-IR for all investigated scenarios are presented in Tables S7 and S8. In Section S2.2, the averaged ($n \geq 2$) profiles of all released volatiles (mg/s) are presented for all investigated scenarios. The profiles show typical trends, which can also be found in the literature.[29, 77, 88]

In Section S2.4, comparisons of yields of CO_2, CO, and CH_4 in relation to conversion temperature between this study and data presented in the literature are shown.[23, 29, 30, 35, 56, 58, 59, 77, 88] The comparison indicates good agreement in the yields and their trend with temperature. The yield of CO and CH_4 up to 500 °C matches previous studies, while yields above that temperature seem to be slightly higher in the present study. The yields of specific compounds obtained in single-particle experiments are sparse in the literature. Therefore, part of the data used in the comparison refers to the results obtained in setups of other types (fluidized or fixed bed reactors), where the heating conditions of particles can significantly differ from those of a single particle unit. As indicated by Williams and Besler, a rise in heating rate (from 10 °C/min to 40 °C/min) contributes the most to the increase in the release of CO_2 (×2) in comparison to other gas components in the pyrolytic gas.[96] It is suspected to be one of the factors that led to elevated CO_2 yields.[77] Part of the results shown for comparison purposes are based on the conversion of smaller particles. The effect of the particle size can be considered another influencing factor. As indicated in a study by Chen et al., where wood particles were converted at 800 °C, an increase in particle size from 0.8 mm to 6 mm led to a rise in the CO_2 yield by ca. 2 wt.%.[26] The yield of CO_2 differs noticeably from the results reported by Anca-Couce et al., who used the same setup. Nonetheless, in the Anca-Couce et al. study, a wood pellet particle was used instead of a single wood particle, which, considering the significant difference in structure and/or composition between both materials, could have affected the yields.[30]

In this study, the evolved H_2O yield was 5 – 8 wt.%, which is close to the amount of pyrogenic H_2O in the study by Anca-Couce et al.[30] H_2O yields in literature are reported to be as high as 20 wt.% in the temperature range of 400 – 500 °C.[29, 55, 56, 88] However, Westerhof et al. showed that for pyrolysis at 500 °C of particles with similar length to those used in the present study, the H_2O

yield should be close to 12 – 14 wt.%.[40] Also, Hoekstra et al. reported H_2O yields at 500 °C in the range of 10 wt.% regardless of the retention time of vapors in the heated zone.[35] Moreover, a broad comparison by Neves et al. does not give a precise answer about the expected H_2O yield.[77] It is suspected that conversion in the single-particle reactor may lead to a difference in the conversion route of a particle, resulting in lower H_2O yields. Another suspicion is that the applied FT-IR analyzer could omit a part of the evolved water for every measurement, while still capturing the overall trend with temperature (assumed constant bias). The objective statement on this matter would require a directed experimental trial. Such research may be demanding since, for permanent gases, ready-to-use mixtures are widely available (which eases the calibration of devices). Unfortunately, such options are not available for water vapor. Moreover, calibration of FT-IR devices for water vapor content requires an adaptation of the quantitation model to changing gas atmospheres. So, if from the experimental setup different atmospheres can be expected, adapted models for each stage/data point had to be applied.

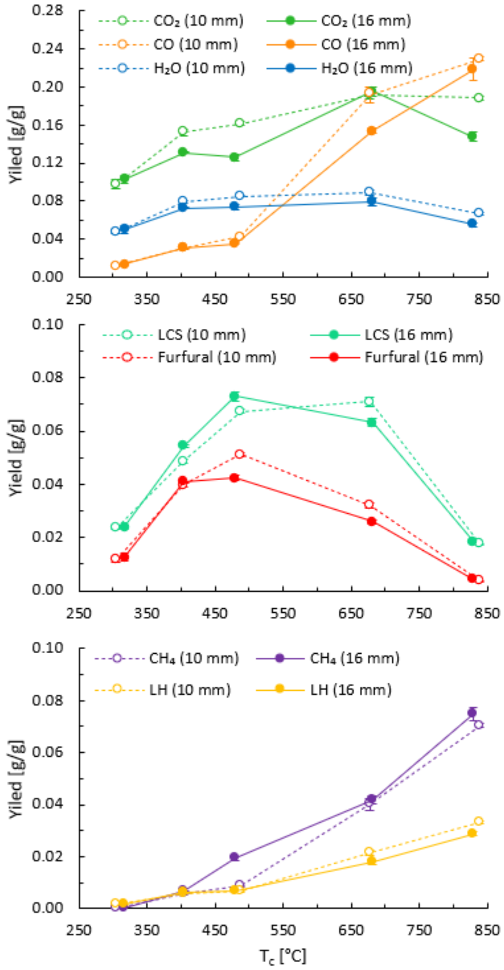

Figure 2. Averaged (n ≥ 2) total release of compounds and their groups as a function of T_C for all investigated scenarios. Top: CO_2, CO, and H_2O; middle: LCS (light condensables) and furfural; bottom: CH_4 and LH (light hydrocarbons).

In general, the FT-IR based profiles and yields presented can be considered representative and reliable for the selected pyrolysis conditions and initial particle properties (see Table S2). Precisely controlled pyrolysis conditions are essential for obtaining representative results in repetitive measurements in a single particle reactor as the process is not continuous. The results indicate a very significant effect of temperature on yields. Nonetheless, although visible, the effect of particle length on yield cannot be clearly demonstrated for specific compounds or their compound groups.

The FT-IR apparatus was not calibrated for all compounds released during the wood pyrolysis process. Therefore, it is suspected that the presence of non-calibrated compounds (e.g., other furanic compounds or phenolics) could affect the measurement in FT-IR with a shielding/shading effect. Such an effect will also be related to the absolute concentration, so its effect will be more profound for a larger sample and higher heating rates. There is a possibility that FT-IR measurement overestimates the furfural yield by the imperfection of the calibration routine. It cannot be ruled out that compounds evolved during the conversion absorb a similar wavelength to the wavelength assigned to furfural (e.g., other furanic compounds or phenolics). Therefore, their presence would artificially increase the furfural yield during the FT-IR assessment.

3.3. Bio-oil composition

The secondary conversion of pyrolysis vapors can occur intrinsically (within the particle) and externally (in the reactor zone).[55] Particles of both lengths were converted under the same conditions, so the observed differences should relate to the impact of the particle length, since the impact of the reactor is assumed to be equal for both particles. The total yields of specific compound groups in relation to T_C for both particle lengths are shown in Figure 3. These data resembled well the temperature-related trends observed for LCS and furfural (cf. Figure 2).

For those groups of compounds, the yields increased up to ca. 480 °C. At higher temperatures, the yields of FU noticeably dropped, while the yields for COX remained constant. At 840 °C, the yields of both compound groups dropped to near zero. The yields of PH showed qualitatively a similar trend with T_C to those of COX, but at the highest T_C the yield of PH did not become negligible. The detection of PAH started above ca. 480 °C, and their yields rose steadily to 680 °C, followed by a sharp increase at 840 °C. Similar trends for the PH and PAH yields with respect to temperature can be found in literature.[31, 33, 35] The results confirm that secondary cracking reactions become more pronounced above 500 °C. However, the observed susceptibility of compounds to undergo thermal cracking is compound-specific, as suggested by other studies too.[34, 37, 95] Due to the sample preparation procedure, it was not possible to obtained a standard deviation over the repetitions (see Section S3.1.). Therefore, an assessment of the repeatability of obtained results cannot be provided.

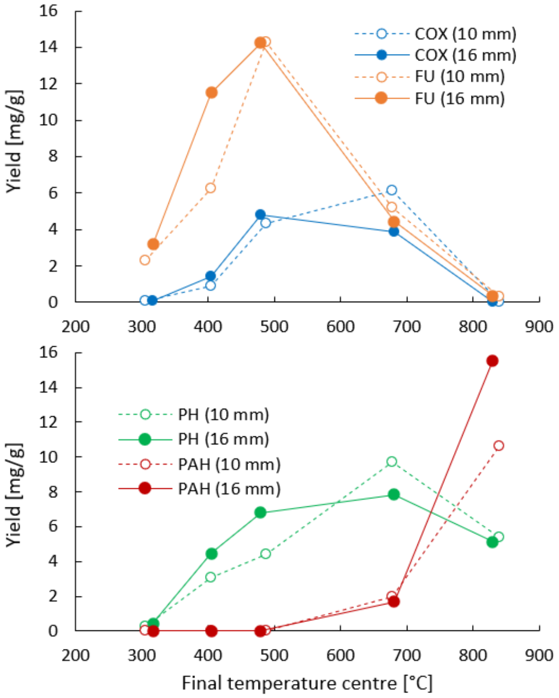

Figure 3. Relationship between the yield of grouped vapor-phase compounds from pyrolysis and T_C for particles of both lengths: 10 mm and 16 mm (top: COX – cyclic oxygenated compounds and FU – furanic compounds; bottom: PH – phenolic compounds and PAHs – polyaromatic hydrocarbons).

The GC-MS/FID and FT-IR data trended similarly for the yields of the pyrolysis vapors versus the length of the particles. Below 500 °C, the yields of all condensable groups were generally higher for the 16 mm particle. It seems to be in contradiction with the expectations, considering, for example, studies of Westerhof et al. and Wang et al., from which one could have expected higher yields for smaller particles.[40, 88] However, in the mentioned studies, the diameter, and hence the heating rate, and not the particle length, was an investigated variable. At 680 °C, the COX, FUR, and PH yields were higher for the 10 mm particle (see Figure 3). A consistent outcome was observed by FT-IR for LCS and furfural (cf. Figure 2). Results from both GC-MS/FID and FT-IR indicate that an increased particle length favored secondary cracking of the primary pyrolysis vapors. The trend agrees with the study of pyrolysis of wood particles at 700 °C by Okekunle et al.[41] At 840 °C, an unclear trend was observed with respect to the particle length, but additional factors were recognized to have an influence on the results (see Section S3.1). In Figure 3, a trend favoring the PAH formation for longer particles is noticeable, especially for temperatures above 680 °C.

The bio-oil yields and mass shares of identified bio-oil species using GC-MS/FID are shown in Table S6. Identified compounds accounted, on average, for ca. 40 wt.% of the total obtained bio-oil per sample. Such a level of compound identification is in agreement with levels previously obtained in the literature.[97-100] As is shown in Table S6, light aromatic compounds like benzene, toluene, or xylene are missing at higher temperatures, while those compounds are present in other studies.[29, 31, 56-59] It needs to be highlighted that all observations, especially those related to the effect of particle length on the secondary reactions of pyrolysis vapors, are based only on the identified compounds (compounds identifiable by GC-MS/FID). Therefore, it cannot be ruled out that the length of the particle had an influence on the evolution of heavy compounds (e.g., lignin-derivatives) in exchange for the lighter compounds (e.g., PH group). If true, such an effect could explain a higher yield of PH compounds for 16 mm particles in comparison to 10 mm particles for T > 500 °C.

It should be stressed that the bio-oil collection method used here was far from optimal (see Section S3.1.) in comparison with other studies.[29, 58] Nonetheless, despite the possible distortion of results by the applied preparation method, the quantitative results matched with reasonable proximity to other results from the literature.[29, 56-59] Details on the subject are provided in Section S3.4. Even though a consistency between sources can be noticed, there is still no certainty about the yields of specific compounds. The latter is mainly related to the application of different setups, wood species, or process parameters (temperatures and/or particle size). Therefore, statements based on the yield of a single component should be made with caution. The trends obtained in this study with GC-MS/FID show satisfactory agreement with FT-IR. Moreover, trends of yields and the extent of secondary cracking with temperature are in agreement with the literature.[29, 35, 56-59] In general, it was noticeable that the length of the particle had an impact on the bio-oil composition (below and above 500 °C). Also, the effect related to the PAH formation was relatively straightforward. Nonetheless, the trends with particle length still remain inconclusive over the relatively broad temperature range investigated in this study. It is presumed that multiple factors, specific at a certain temperature, could affect the results. Additionally, the imperfection of the applied experimental method (like difficulties in bio-oil measurement or lack of identification of heavy tars) could not account for information that would allow for unambiguous statements. More directional experimental work is necessary to make a conclusive statement about the effect of particle length on the yield of evolved pyrolysis vapors and provide a quantitative correlation.

3.4. Mass and elemental balance

As other studies indicate, pyrolysis at 500 °C of wood particles with a similar size and shape to those investigated in this study should produce an organic liquid fraction (water-free bio-oil) with a yield close to 40 wt.% on a feedstock basis.[40, 88] Combined results from FT-IR (LCS + furfural) and GC-MS/FID measurements at T_c = ca. 480 °C showed a total organic yield of ca. 20 wt.% (excluding furfural and compounds with evaporation temperatures lower or comparable to isopropanol). It suggests that the collection, preparation, and analysis of liquid samples led to quantification losses of ca. 50 wt.% of the organic liquid fraction. In a relative manner, this value can be assessed as high. However, the mass of the wood particle was in the range of 300 – 500 mg, so at optimal conditions, 120 – 200 mg of the organic liquid fraction could theoretically be obtained. Considering the extensiveness of the pyrolysis setup and the number of preparation steps (see Section S3.1.), such a loss of quantification seems unavoidable. Another point is that the analysis did not include heavy tars, which adds to the missing mass.

Mass and elemental balances (C, H, and O) for the pyrolysis of beech-wood pellets are presented in Figure 4 (samples assigned as in Table 2), and details are given in Section S4. The balances include feedstock mass, char mass, and summed masses of gas/vapor phase compounds as quantified by FT-IR. The mass of individual vapor-phase compounds quantified by GC-MS/FID were excluded from these balances for a number of reasons. Firstly, the total bio-oil yield exceeded 5 wt.% only in a few cases, but its identified part did not, in any scenario. So, the mass quantified by GC-MS/FID represented only a minor fraction of the total volatile mass. Moreover, due to the preparation procedure, measurement of the bio-oil from each replicate was not possible, and the obtained GC-MS/FID results did not include standard deviation. Additionally, in any scenario, the mass of the collected bio-oil did not exceed 100 mg (even under the most favorable conditions). Such mass did not allow for replicable, conventional elemental analysis of the bio-oil (even for bio-oil pooled from 3 replicates).

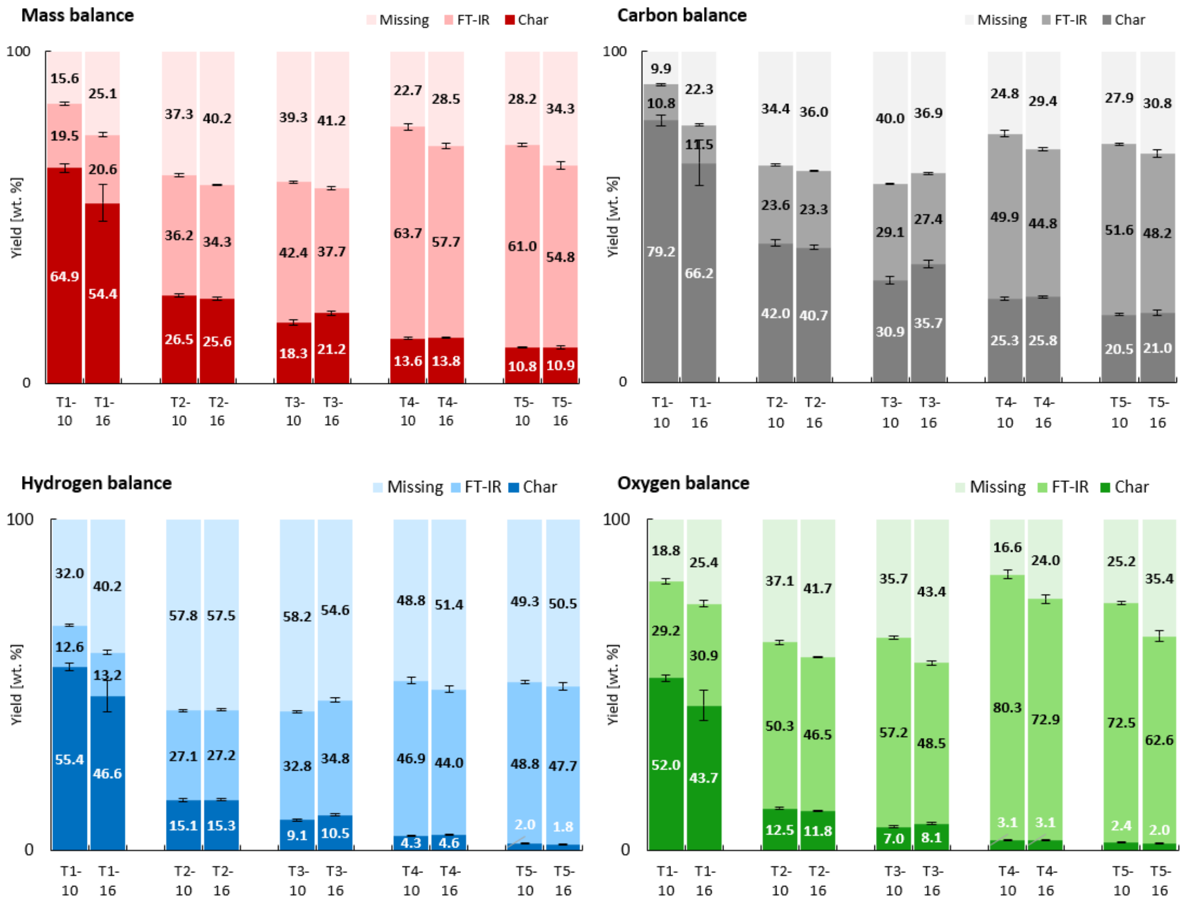

Figure 4. Mass balance (top left) and carbon (top right), hydrogen (bottom left), and oxygen (bottom right) balance of averaged chars and averaged FT-IR (gas-phase) results (both n ≥ 2) from pyrolysis of beech wood particles.

The share of missing mass increased from 300 °C to 480 °C, decreased at 680 °C, and increased again at 840 °C. While char yields showed a typical trend with T_c, the changes in missing mass by FT-IR had the most substantial effect on the observed trend. A temperature around 500 °C is considered as the optimal temperature for turnig wood into bio-oil.[88] A significant part of bio-oil was outside of the quantification capacity of this study, up to 480 °C, an effect which is presumed to be the main factor adding to the missing mass. With a further increase in temperature, more bio-oil constituents (i.e., volatiles) crack toward non-condensable gases, which was within the detection and quantification by FT-IR. This is in agreement with the increase in mass quantification and consequent reduction in missing mass at 680 °C. It is suspected that at 840 °C, the drop in total mass quantification was caused by the presumed elevated formation of monoaromatic hydrocarbons (MAHs) and PAHs as well as the increased formation of hydrogen gas.[31, 33, 77] These compounds were indeed not detectable by FT-IR, resulting in a consecutive increase in the share of missing mass.

Up to 500 °C, the proportion of the mass represented by FT-IR was similar for particles of different lengths. Slight deviations were presumingly related to differences in process conditions (see Table 2). However, above 500 °C, the 16 mm particle showed a noticeably lower proportion of the total mass, carbon, and oxygen quantified by FT-IR. At 840 °C, the char yields had similar values for particles of different lengths, while the carbon yields were higher for the 16 mm particles (difference by 0.51 ± 0.08 wt.% of C). Since PAHs are the precursors of soot, their high formation might cause carbon (soot) deposition in the pores of the material.[36, 37] This would lead to an increased carbon content of the obtained chars. Considering the elevated formation of PAH for 16 mm particles at 840 °C (see Section 3), it may be expected that the increase in particle length leads to greater secondary cracking of the vapors released and the consecutive formation and deposition of solid carbon. Therefore, the concentration of PAHs in pyrolytic vapors may be considered a good indicator of the deposition of solid carbon formed secondarily in the char structure.

The missing mass of pyrolysis products quantified with the methods used seems relatively excessive (between 16 and 41 wt.%). Nonetheless, the result is within the upper range of mass missing in comparison to prior research on the same single-particle pyrolysis setup.[30] Among the investigated elements, carbon showed the best mass balance closure, while the missing mass was the highest for hydrogen (from 32 to 58 wt.% H of feedstock). Another study carried out with the same setup also observed a significant missing mass of hydrogen, and the high missing mass of hydrogen there related to a lack of direct hydrogen gas measurement (but in the mentioned study, bio-oil compensation was applied).[30] Other studies indicate that the mass of hydrogen released up to 500 °C is relatively low (not more than ca. 1.5 wt.% H of feedstock). The yield of hydrogen gas rises sharply above 500 °C, and at 800 – 850 °C, it may account for even 10 wt.% H of feedstock.[29, 55, 59, 77] Therefore, it would be incorrect to attribute the lack of hydrogen gas measurement in the outlet gas stream as the sole factor leading to a high missing hydrogen mass. In this study, where bio-oil compensation was not applied, unquantified bio-oil can be referred to as the main factor in the missing hydrogen. However, two factors already mentioned in Sections 3.2 and 3.3 also need to be highlighted with regard to missing mass and hydrogen. The first is the incomplete quantification of the mass of H_2O released which, at 480 °C, can be estimated at ca. 5 – 10 wt.% of the total mass of feedstock. The second, and a less obvious factor, is a presumed overestimation of furfural by FT-IR. Overestimation could lead to an apparently better closure of the mass balance but could simultaneously create a bias not only in the hydrogen yield, but also in the carbon and oxygen yields.

3.5. General structural changes

The trends for the true density, bulk density, and porosity with respect to T_c for particles of different lengths are shown in Figure 5. Both true and bulk density have a relatively low standard deviation, while the porosity had a more noticeable uncertainty. The trends for both particle lengths for true and bulk density are in agreement with the literature data.[101, 102] Apart from a notable deviation in true density at 840 °C, both particles did not show a significant difference in bulk density and porosity values at any T_c. It seems that for parameters such as the density and porosity, the 6 mm length difference between particles was insufficient to create a substantial effect. The discrepancy in the true density at the end of the temperature range may be attributed to soot deposition, but further validation needs to warrant this in the future.[2]

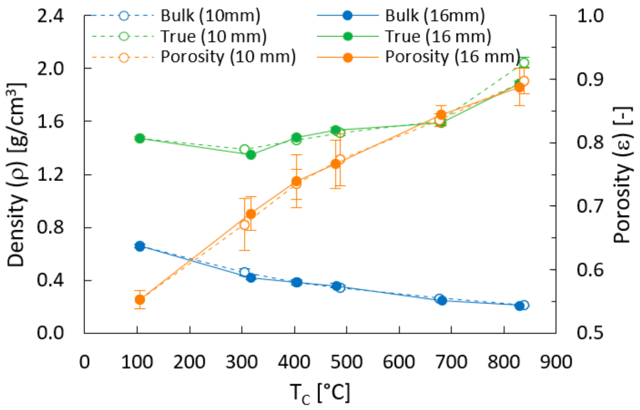

Figure 5. Bulk density, true density, and porosity of char particles as a function of T_c for particles with a length of 10 mm and 16 mm.

The dimensional changes in the longitudinal (L), radial (R), and tangential (T) dimensions of a particle, as well as the volume change (V) are presented in Figure 6 as a function of the final T_c. Up to ca. 480 °C, the dimensional and volume changes of particles with both particle lengths were relatively similar. Above this T_c, the dimensional changes started to be affected by the initial particle length. For both lengths, the dimensional change of the radial and tangential direction caused a change in the overall geometric shape of particles from cylinders to elliptic cylinders. Conversely to the modeling studies, the particles did not show a noticeable deviation in radial and transverse dimensions between the top/bottom and the middle of the particles.[19, 103]

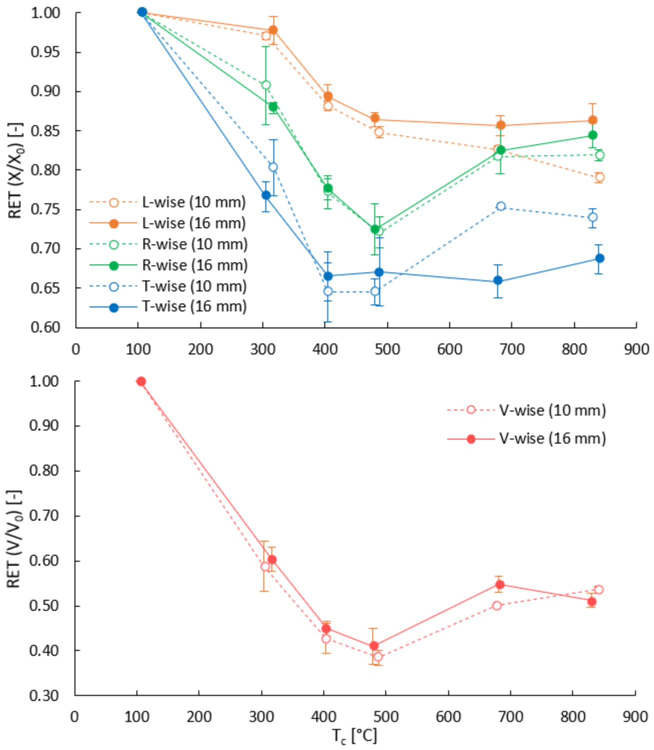

Figure 6. Relationship between dimension/volume retention factor (RET, as in Eq. S8) (top – dimensions, bottom – volume) and T_c for all investigated scenarios (dashed line – 10 mm, solid line – 16 mm).

Also, above 480 °C, cracks and fissures in the particles started to become profound. It was observed that they commonly started on the growth rings of the wood, causing a layering of the structure and deformation in the radial direction (see Figure S19). The cracks and fissures created additional lower-resistance pathways through which, theoretically, evolved vapors could escape from the particle. Hence, the formation of fissures should affect secondary cracking (providing a shorter vapor escape route) or possibly the conversion by changes in heat transfer within the particle. Additionally, structural deformation patterns within particles should be specific, rather than homogenous for all particles within a given pyrolysis scenario. So, the occurrence of deformation should result in a more visible deviation in the results, in terms of length or volume, as well as the amount and composition of volatiles and gases released. No such effect was observed in the FT-IR results (see Figure 2).

Theories on the origin of the anisotropic shrinking of wood during pyrolysis can be found in the literature.[64, 65, 87] The observed changes in the longitudinal direction with temperature and its asymptotic trend, together with the changes in the radial and transverse directions, are consistent with these theories. An ambiguity can be observed in the literature regarding the increase in the particle dimension with temperature.[64, 65, 104-107] Davidsson and Pettersson stated that differences in heating rate might explain this, and the increase in the tangential dimension in this study may be related to the fact that the cracking or layering was not observed on medullary rays.[106] It is assumed that temperatures above 500 °C and sufficiently high heating rates could create mechanical stresses within the particle and lead to its (physical) cracking at the weakest structural points. Given that the cracks most often appear on the growth rings (annual rings), it is suspected that these parts of the wood may have a chemical composition that, during pyrolysis, is more susceptible to thermal breakdown and results in a discontinuity of the structure. However, due to insufficient information available in the literature about the difference in composition between wood and its growth rings, the hypothesis cannot be confirmed at this moment.

Above T_c = ca. 480 °C, some of the particles cracked into pieces during conversion, which was also observed in previous studies.[21, 106-108] An example of this situation can be found in the video provided in Supporting Information 2. Such cracking was often observed at T_c = ca. 680 °C, where the particles also exhibited the greatest brittleness and were most prone to damage upon removal from the reactor. Literature indicates a minimum in crushing strength, so the weakest mechanical durability of bio-based chars corresponding to those produced between 550 °C and 750 °C.[109, 110] It has been ascribed to an offset in the minimum ductility at 550 °C, followed by a re-gaining in hardness and elasticity of the material, both at 750 °C.[105, 111] The origin of such mechanical behavior is rooted in the changes that the carbon matrix structure undergoes and, since the subject is beyond the scope of the present study, further discussion will be omitted.

The change in the volume of the particle had a similar trend for both particle lengths, with a reduction close to 40 vol.% up to 480 °C. At higher temperatures, the volume increased, and cracking and fissures were more profound. The particle volume changes should also be reflected in its bulk density, but the latter was not observed (see Figure 5). In this study, the bulk density measured by MIP refers to the mass divided by the volume of the particle, excluding pores larger than 500 μm (see Section 2.8). Assuming that the physical cracking as such does not affect the bulk density, the main structural defects appearing in particles above T_c = 480 °C do not relate to the overall porosity. Therefore, the increase in particle volume in this study was purely geometric. It should be pointed out that if the occurrence of structural deformation in the particles cannot be ruled out during conversion, the bulk density derived from the geometric assessment (i.e., the particle volume calculated from the particle dimensions) will be subject to significant error. If the risk of structural deformation appears, more advanced methods, such as MIP, should be applied for volume assessment.

3.6. Analysis of char structure and morphology

SEM images of chars from 16 mm particles for all T_c are presented in Figure 7. Particular interest was devoted to changes in the vessels/tracheids and the pits visible on the images, and these were also assessed with the MIP experiments. The roughness of the edges on the particles obtained at T_c = ca. 320 °C was relatively low, and the edges looked soft. The visible channels were slim, and pits were barely visible. At 320 °C, the char structure resembled virgin wood. At higher temperatures, the morphology of the particles changed significantly. From 400 °C to 480 °C, the edges of the material became sharper, and the channels became wider with more noticeable pits. The most profound changes were observed after pyrolysis at temperatures of 480 °C to 680 °C. Here, the surface of the material became smooth and edges sharp. Lines of the vessels/tracheid channels became strongly visible with relatively wide channels and thin walls. Pits became strongly visible at that temperature and had a wider opening. A further increase to 840 °C elevated the observed effects at 680 °C, where the channel became wider, making the walls thinner.

Davidson and Pettersson observed a similar behavior of the morphologies of the chars as analyzed by SEM.[106] They assigned the changes observed between 770 °C and 850 °C to elastic deformation (stretching and relaxation). Stretching and volume reduction occurred in their study up to 500 °C, above which the structures "swelled" and increased in volume. In the mentioned study, the phenomenon was observed only above 770 °C and not above 600 °C. Therefore, it is suspected that their observation might be related to the selection (possibly) of non-representative SEM images. The SEM images in this study do not indicate any stretching or relaxation of the structures. The images confirmed our hypothesis that the particle expansion was not volumetric but related to particle geometry. Therefore, the increase in particle volume ("swelling") derived from measurement with basic tools (e.g., ruler or digital micrometer) does not translate directly to the bulk density of a particle (defined as a porous structure with pores that do not exceed 0.5 mm).

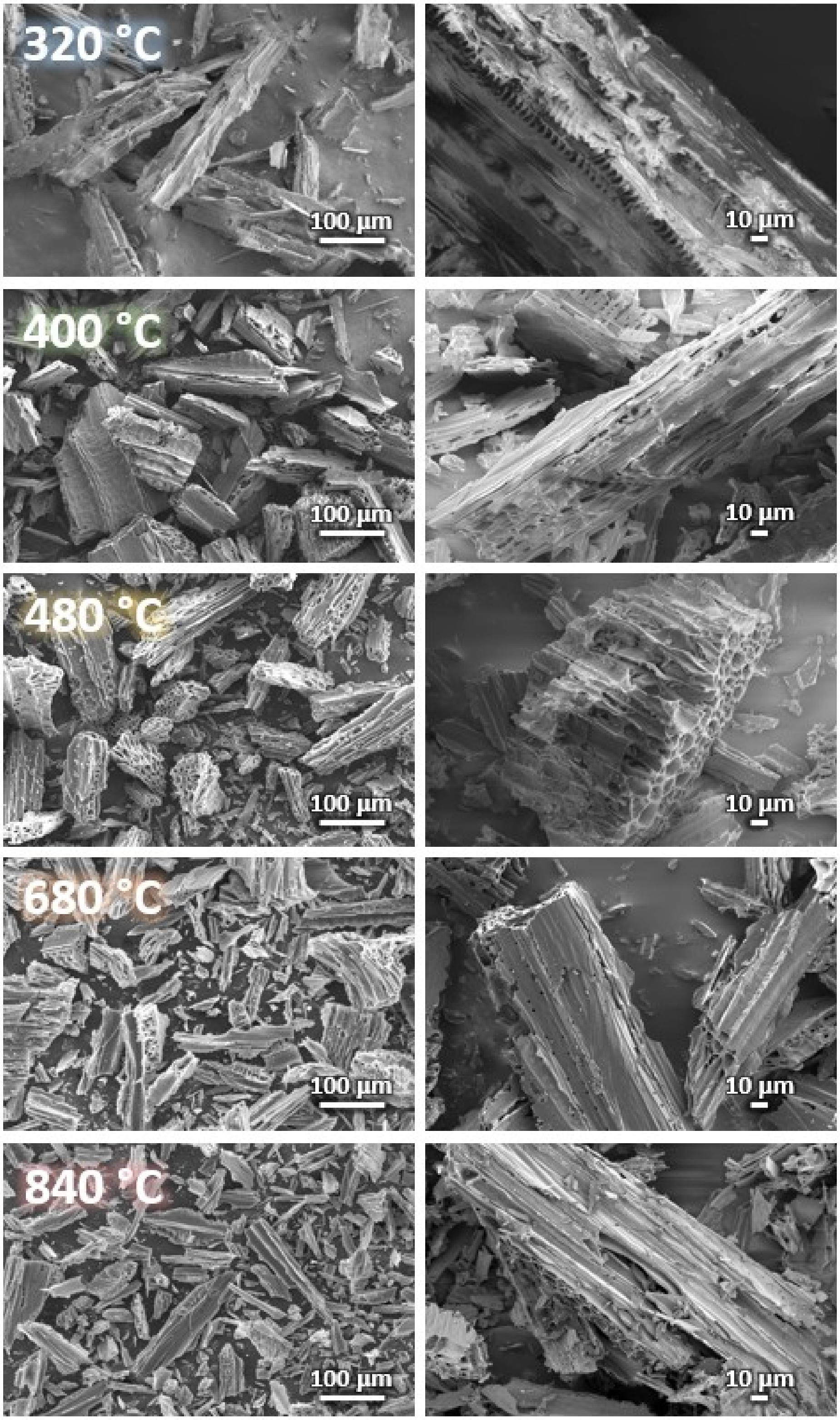

Figure 7. SEM images of beech wood chars obtained between 320 °C and 840 °C for a 16 mm particle in two magnifications (left – ×100, right – ×500).

3.7. Specific effects on char porous texture

A detailed description of changes in the PSD down to 20 nm is provided in Section S5.5. These changes provide insights into the mechanisms behind the evolution of micro- and meso- pores as a function of conversion temperature. However, such a discussion needs to be held with caution. The precise location of the peaks for the micro- and meso-porosity distribution strongly depends on the applied calculation methods (e.g., kernel), which holds true even in this study, where the most novel approach was applied. In this regard, the use of complementary analytical methods such as small angle X-ray scattering (SAXS), transmission electron microscopy (TEM), and absorption of specific molecules can be useful for the validation of the gas adsorption results.[49, 112-115] Nonetheless, the parameters derived from micro- and meso- PSD (e.g., V_{pore} and SSA) can serve as indicators of the structural changes within the selected pore range. They are validated by theoretically embedded estimators (e.g., BET or Dubinin-Radushkevich calculation methods), so their use to describe changes should not be biased.[70] Conversely, the calculation of the macroporous PSD is based on a straightforward, well-proven theory. Therefore, there is no risk regarding miss-assignment of the peak location if the right material properties are used in the calculation procedure. Nonetheless, a validation of PSD for the material macrostructure can be made with the results of 3D reconstructions of X-ray micro-computed tomography (known as μ-CT or XCT).[50, 51]

For quantitative assessment of changes in PSD with T_c, the V_{pore} and corresponding SSA were divided into specific ranges (see Section 2.8.). The V_{pore} as a function of T_c for all investigated scenarios are presented in Figure 8 and, in addition, Tables S9 and S10 report the values of V_{pore} and SSA, respectively. The volume of the smallest pores (Mi-S, 0.35 nm – 0.7 nm, see Table 3) increased for both particle lengths from 300 °C to 480 °C, decreased from 480 °C to 680 °C, and then increased again from 680 °C to 840 °C, as seen from Figure 8. The volume of slightly larger pores (Mi-L, 0.7 nm – 2 nm) increased up to a temperature of 680 °C, after which it decreased to some extent. The shape of the Mi-L curves resembles the shape of the curve for the CO_2 yield of the 16 mm particle (cf. Figure 2). Both, Me-S (2 nm – 50 nm) and Me-L (50 nm – 100 nm) trended downwards with increasing pyrolysis temperature. The Ma-U (0.1 μm – 5 μm) trended upwards until a limiting temperature. Also, an upward trend was noticeable for Ma-S (5 μm – 30 μm). For Ma-M (30 μm – 75 μm) and Ma-L (75 μm – 500 μm), the pore volumes increased significantly, especially at the highest temperatures. The dependency on the particle length was negligible or absent for most of the pore diameter ranges. Nonetheless, the Mi-S volume was significantly higher for chars prepared from 10 mm particles than for 16 mm particles.

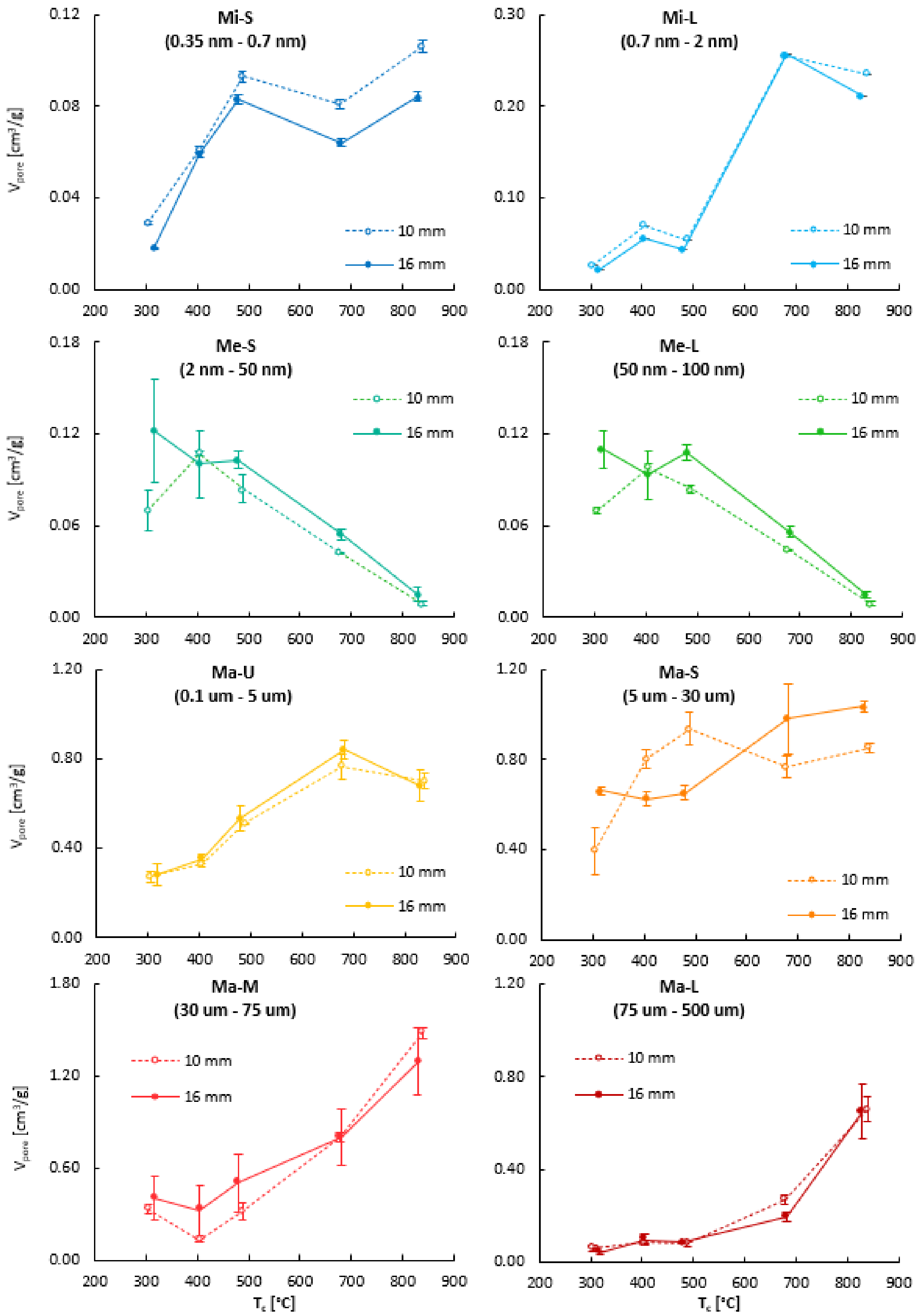

Figure 8. Averaged (n ≥ 2) V_{pore} for specific pore size ranges and as a function of T_c for all investigated scenarios (dashed line – 10 mm and solid line – 16 mm).

Virgin beech wood is composed of basic structural units with distinctive diameters, such as: vessels from 5 μm to 100 μm, tracheids/fibers from 15 μm to 20 μm, and pits from 4 μm to 11 μm.[116, 117] The smallest structures (below 5 μm) relate to micro-pits in radial/transverse direction, micro-voids, and cell wall capillaries.[44] The pore volume trends for Ma-U/S/M/L can be assigned to changes related to those structural formations in wood. Changes in the PSD for a specific particle with temperature are shown in Figure S20 (results of each repetition from Hg porosimetry) and Figure S21 (separate PSDs of the micro-, meso- and macro-pore range). Additionally, Figure S22 presents complete PSDs from 0.35 nm to 500 μm for all investigated scenarios, which allows for a visual assessment and comparison of changes in the pore volume over the whole pore size range. The increase in conversion temperature distinctively leads to an increase in the size of the smallest structures and shifts the peak location from 0.05 μm – 0.2 μm to 0.5 μm – 4 μm. A similar result was observed by Pfriem et al.[45] The widening of the formations (probably due to the thinning of the walls) started to be noticeable above 480 °C, as shown in the PSDs and SEM results. It needs to be highlighted that, above 500 °C, PSDs in Figures S21 and S22 do not show any reduction of peak height or width (for pores with sizes up to 500 μm). It additionally confirms that the structural deformations leading to geometric "swelling" are related to structures that have not been counted as pores (such as macroscopic cracks and fissures).

The contribution of pore volume from a specific pore group to the total pore volume, presented in Figure 9, indicates that the macropore share did not drop below 80 vol.% in any investigated scenario. The macropore volume reached its minimum at ca. 400 °C, and at 840 °C, it accounts for ca. 90 vol.%. The share of mesopores with T_c drops from an initial value ca. 15 vol.% to a few vol.% at 840 °C. The share of micropores increases from an initial few vol.% to ca. 10 vol.% at 680 °C, followed by a slight drop at 840 °C. Results indicate that thermo-physical parameters (effective thermal conductivity, permeability) of chars should be related to parameters derived from the macroporous structure (e.g., average pore diameter). Additionally, it should be considered that vessels and tracheid have cylindrical/cuboid shapes, and their ratio of length to diameter may vary significantly, e.g., the ratio for beech wood vessels is ca. 7000, and for tracheids, it is 50.[117]

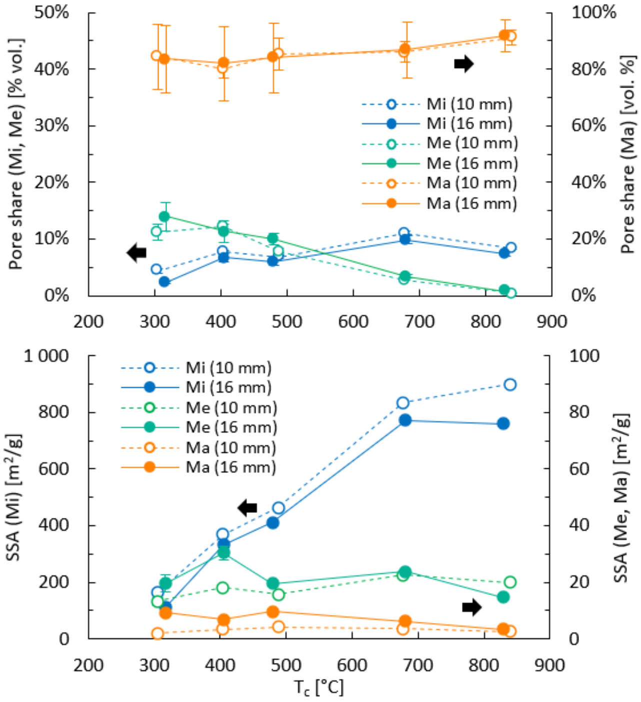

Figure 9. Relationship between volume share of pores within specific size ranges (top) and SSA of specific pore size ranges (bottom) and the final temperature at the particle center for both particle lengths (dashed line – 10 mm and solid line – 16 mm).

The micropore volume directly corresponds to the highest share of the SSA for investigated materials. Therefore, SSA derived from other pore groups will be significantly lower, if not negligible (as for macropores). The chars prepared from 10 mm particles showed a higher microporous SSA than those from 16 mm particles. The difference was relatively constant up to 480 °C but increased slightly at 680 °C, and, at the final temperature of 840 °C, it became significantly visible. The SSA of macropores and mesopores stayed relatively low and constant regardless of the applied temperature. A noticeable exception here was the higher value of the mesoporous SSA for the chars from the 10 mm particles at 840 °C as compared to that derived from the 16 mm particles.

3.8. Tradeoffs and char tailoring for a given application

The most relevant parameter for the application of carbon material in (electro-)chemical and adsorption processes is the PSD in the micro-mesopore range and the related SSA. However, pyrolytic carbons are rarely used directly for these applications, while their derivatives, activated carbons, have a wide industrial application. It should be pointed out that a process for producing activated carbon precursors, so-called carbonization, takes place at lower temperatures (400 – 500 °C). According to the DIN EN 1860-2, the charcoal (precursor) must contain 80 wt.% of fixed carbon (irrespective of other parameters), which corresponds to a production temperature close to 500 °C.[118] This corresponds to the Food and Agriculture Organization of the United Nations (FAO) recommendation for industrial charcoal production.[119] Next, physical activation, commonly applied in industry, takes place at temperatures between 800 °C and 1200 °C using flue gases from natural gas combustion (also with an additional injection of steam) as an activating agent.[120] While chars for use in pollutant adsorption applications may not always require activation, it is required when the material is intended to be used as a supercapacitor. Chemically activated carbon (e.g., KOH or K_2CO_3 at 400 –700 °C) is often preferred for such applications. Materials intended to be used in electrochemistry have rigorous requirements regarding irreversible capacity, voltage hysteresis, and cycling stability. The mentioned properties directly relate to the chemical composition of the material, regardless of the PSD. For application in supercapacitors, the material must have most of its SSA in the 1.2 – 2 nm pore region, as smaller pores are not easily accessible to ions.[120, 121] The relationship with pollutant removal (pharmaceuticals or heavy metals) is not yet fully understood, since multiple adsorption mechanisms are at play and depend on the chemistry of the carbon surface in addition to the properties of the absorbed molecules.[3, 122-125] For this purpose, it can be assumed that the SSA must be located in the pore size range above the size of the absorbed molecules (e.g. for pharmaceuticals compounds), while for heavy metals, the entire microporous range of the SSA can be considered usable.

Considering that the precursor for activated carbon should have the highest PSD in the range of Mi-L (0.7 nm – 2 nm), the results show that it might be better to carbonize the material at higher temperatures (around 840 °C), since the SSA obtained for that specific range was the highest at those temperatures. The risk of pore closure/collapse due to re-organization of the carbon structure at higher temperatures cannot be ruled out.[126, 127] Therefore, higher temperatures cannot be recommended in this study as they could lead to the opposite of the desired result. However, if the yield of the pores (char yield × pore volume) in the Mi-L region would be considered, then the highest yield of pore volume per initial biomass is obtained at 680 °C. Also, the mesoporous volume, which acts as a micropore connector, is not the lowest at this temperature. Furthermore, at 680 °C, relatively short particles should be used for production to reduce carbon deposits in their structure. It is questionable whether such a tradeoff is favorable, given that between 500 °C and 700 °C, the char yield decreases by ca. 3 – 5 wt.%. Another question is whether it is worth producing char intended for activated carbon at a temperature required by standards if, in any case, the char will be heated above this temperature during activation. One might also ask whether producing char at temperatures above 500 °C would not reduce the energy needed to crush/grind the material, and thus balance out total energy requirements. Answering these complex questions is beyond the scope of this work.

Bio-based chars (biochar) can straightforwardly be used as a soil amendment after fulfilling restrictions imposed by the International Biochar Initiative (IBI) and European Biochar Foundation (EBC) standards.[128, 129] In terms of general properties, biochars must have a H/C_{org} lower than 0.7, which, for wood, relates to production temperature equivalent of 350 – 400 °C. An additional point to be mentioned is the chemical stability of chars, which reflects the carbon sequestration potential. Considering only abiotic factors, higher pyrolysis temperature leads to higher char stability, so the trend with temperature is very straightforward.[130] Nonetheless, the mass loss against temperature must also be considered for estimating sequestration potential per initial quantity of biomass.

The standards indicate that the concentration of PAHs within the char must be relatively low. PAHs formation depends on the pyrolysis temperature, where temperatures above 500 °C strongly enhance their formation.[33, 37] Studies of the subject indicate that temperature above 500 °C leads to an increase in PAHs in chars.[131, 132] It needs to be highlighted that PAHs are formed not only within the particle (intrinsic PAHs) but also in the reactor zone (via secondary reactions of vapors).[55] Therefore, elevated concentrations of PAHs in the collected bio-oil do not necessarily indicate their occurrence in char. When the temperature is favorable for PAHs formation, the exposure time of particles to vapors should be minimized, not to cross-contaminate char, which can be obtained by, e.g., elevated sweep gas flow. Such an action should also lead to a reduction of the intrinsic retention of vapors within the char due to the enhancement of their convective removal from the surface. Nonetheless, the intrinsic retention time depends also on the particle size, especially length. As this study shows, for similar conditions in the reactor zone (flow, temperature), the conversion of the longer particle led to elevated PAHs yields (and possible higher soot deposition related to it). It is suspected that a partial cause of such a result is the higher absolute pore volume of longer particles, where more residual vapors stay after conversion (e.g., in areas close to the center of a particle), so more vapors are exposed to conditions favorable to form PAHs (and soot). Therefore, it can be stated that a reduction of the PAH formation, as well as a reduction of risk related to char contamination with PAHs, can be obtained by a reduction of the particle size. However, temperature still needs to be pointed out as a critical factor.

Macropores are critical for chars in soil applications. As far as water retention is concerned, pores with a diameter >75 μm allow the movement of water in the soil but may cause faster drainage. Pores with diameters ranging from 5 μm to 30 μm and from 30 μm to 75 μm are related to water retention in the soil, but only the latter ones retain water that is entirely available to plants.[133, 134] In smaller pores, < 5 μm, water is also retained but is not available to plants. However, as they retain moisture, they can provide a habitat for beneficial microbes, such as phosphorus-solubilizing bacteria whose size ranges from 0.2 μm to 10 μm (e.g., *Bacillus megaterium*, approx. 4 μm long and approx. 1.5 μm in diameter).[135] The results show that volume and yield per biomass of pores, which retain plant available water, drops slightly from 300 °C to 500 °C and rises rapidly up to 840 °C. However, the water-draining pores also show a similar tendency. For pores with a diameter from 0.1 μm to 30 μm, the best yield per biomass is obtained at 300 – 400 °C, and it drops noticeably with a further increase in pyrolysis temperature. The influence of the particle length does not play a significant role for those structures. Overall, in the case of the soil applications of char, a conversion temperature of 700 °C can be advised to obtain favorable water retention properties. Nonetheless, particular attention must be paid to PAHs content in the char when conversion is conducted at such an elevated temperature. On the other hand, the temperature should not exceed 500 °C if char is considered as a bacterial habitat.

The PSD results obtained, and therefore, the recommendations refer to beech wood. However, given the similarity in composition and structure to other wood species, the recommendations should also be valid for other wood species.[117] Further research should be carried out to confirm this assertion and assess whether the trends observed are accurate for different types of biomass (fruit stones, shells, husks, and herbaceous biomass).[49]

5. Conclusions

In this study, it has been shown that secondary cracking of vapors evolved during pyrolysis of beech wood started to become relevant above 500 °C. The compound-specific behavior of the phenomena was confirmed. The effect of particle length on the secondary cracking was ambiguous for specific compounds, so a quantitative relation for all investigated compounds could not be provided. Overall, the results showed an acceleration of cracking with conversion temperature (on average for both particles), a decrease in condensable vapor (without PAHs) yield of 14.4 ± 1.0 wt.% between 480 °C and 840 °C. Between 680 °C and 840 °C the increase of the PAHs yield was higher for 16 mm particles than for the 10 mm ones (×9 and ×5, respectively). The higher PAHs formation for 16 mm particles at 840 °C promoted higher carbon yields in chars (by ca. 0.25 wt.%) and reduced microporosity (specific surface area, by ca. 140 m^2/g). Interestingly, the effect of particle length was pronounced in the micropores region but negligible in the macropores range. The increase in the geometrically assessed volume of the particle was not uniform volumetrically, but it was related to the appearance of cracks. Furthermore, the term “swelling” should be used cautiously in further studies. A detailed assessment of the pore morphologies of the chars indicated reliable, quantitative trends with conversion temperature, which can be implemented in subsequent modeling works.

As observed in this study, the low-temperature conversion (below 500 °C) had an impact on the pore morphology. Therefore, despite the fact that the study presents an example of a comprehensive approach, even more detailed studies on the subject are recommended. Future studies should enhance investigation by providing a more detailed assessment of the release of vapors, especially heavy compounds. Those insights will extend the understanding of the mechanisms behind the secondary reactions of vapors, also at high temperatures, which relate to PAHs and secondary char/soot formation. With such information, the quantifiable effect of the particle size (lengths and radius) on the pore morphology could be derived.

The study proves that despite the difficulty of assessing the various interconnected phenomena involved in biomass pyrolysis, it is possible to understand the reproducible production of tailored-made chars. Of course, these efforts will have to be combined with application trials, in order to validate the tailoring procedures. Additionally, the comprehensive dataset obtained in this study lays the foundations for extending the research to Computational Fluid Dynamic (CFD) modeling of single-particle pyrolysis. In doing so, the particle behavior can be represented with greater accuracy, which could lead to an improved understanding of the process and further optimization of char tailoring. This will be the subject of Part 2 of our forthcoming work.

ASSOCIATED CONTENT

Supporting Information 1 – Images of the experimental setup and additional experimental details, materials, and methods (PDF)

Supporting Information 2 – Video of wood particle explosion during single-particle pyrolysis at a conversion temperature of ca. 840 °C (MP4 file)

AUTHOR INFORMATION

Corresponding Author

* Department of Green Chemistry and Technology, Faculty of Bioscience Engineering, Ghent University, Coupure Links 653, 9000 Gent, Belgium, Przemyslaw.Maziarka@ugent.be

Author Contributions

The manuscript was written through contributions of all authors. All authors have given approval to the final version of the manuscript.

P.M. - Conceptualization, Methodology, Investigation, Formal Analysis, Visualization, Writing – original draft, N.K. - Resources, Writing – review & editing, A.D.A. - Investigation, Resources, Writing – review & editing, V.F. - Investigation, Resources, Writing – review & editing, A.C. - Investigation, Resources, Writing – review & editing, P.J.A. - Formal Analysis, Writing – review & editing, N.H. - Investigation, Resources, Writing – review & editing, W.P. - Writing – review & editing, A.A.C. - Conceptualization, Methodology, Supervision, Writing – review & editing, J.J.M. – Funding acquisition, Supervision, Writing – review & editing, F.R. - Conceptualization, Methodology, Resources, Funding acquisition, Supervision, Writing – review & editing

Funding Sources

The research was supported by the Brisk 2 and Green Carbon project. The Brisk 2 project has received funding from the European Union's Horizon 2020 research and innovation program under grant agreement No 731101. The Green Carbon project has received funding from the European

Union’s Horizon 2020 research and innovation program under Marie Skłodowska Curie grant agreement No 721991.

Notes

The authors declare no competing financial interest.

ACKNOWLEDGMENT

The authors would like to sincerely thank Prof. Dr Jesús María Arauzo Pérez from Universidad de Zaragoza (Spain) and Dr Eng. Mariusz Wądzyk from AGH University of Science and Technology (Poland) for their assistance in the GC/MS-FID assessment of bio-oils. Additionally, the authors would like to sincerely thank Dr Jacek Jagiello from AGH University of Science and Technology (Poland) for lending the authors access to the full version of the SAIEUS Program (Version 3.2).

REFERENCES

1. Wang, J.; Wang, S., Preparation, modification and environmental application of biochar: A review. *Journal of Cleaner Production* **2019,** 227, 1002-1022.
2. Li, X.; Zhang, J.; Liu, B.; Su, Z., A critical review on the application and recent developments of post-modified biochar in supercapacitors. *Journal of Cleaner Production* **2021,** 310, 127428.
3. Jeguirim, M.; Limousy, L., Char and carbon materials derived from biomass : production, characterization and applications. In First edition ed.; Elsevier Amsterdam: Amsterdam, 2019.
4. de Coninck, H.; A. Revi; M. Babiker; P. Bertoldi; M. Buckeridge; A. Cartwright; W. Dong; J. Ford; S. Fuss; J.-C. Hourcade; D. Ley; R. Mechler; P. Newman; A. Revokatova; S. Schultz; L. Steg; T. Sugiyama, Strengthening and Implementing the Global Response. In: Global Warming of 1.5°C. An IPCC Special Report on the impacts of global warming of 1.5°C above pre-industrial levels and related global greenhouse gas emission pathways, in the context of strengthening the global response to the threat of climate change, sustainable development, and

efforts to eradicate poverty. In *IPCC - The Intergovernmental Panel on Climate Change* MassonDelmotte, V., P. Zhai, H.-O. Pörtner, D. Roberts, J. Skea, P.R. Shukla, A. Pirani, W. Moufouma-Okia, C. Péan, R. Pidcock, S. Connors, J.B.R. Matthews, Y. Chen, X. Zhou, M.I. Gomis, E. Lonnoy, T. Maycock, M. Tignor, and T. Waterfield, Ed. 2018; pp 313 - 443.

5. Bachmann, H. J.; Bucheli, T. D.; Dieguez-Alonso, A.; Fabbri, D.; Knicker, H.; Schmidt, H.-P.; Ulbricht, A.; Becker, R.; Buscaroli, A.; Buerge, D.; Cross, A.; Dickinson, D.; Enders, A.; Esteves, V. I.; Evangelou, M. W. H.; Fellet, G.; Friedrich, K.; Gasco Guerrero, G.; Glaser, B.; Hanke, U. M.; Hanley, K.; Hilber, I.; Kalderis, D.; Leifeld, J.; Masek, O.; Mumme, J.; Carmona, M. P.; Calvelo Pereira, R.; Rees, F.; Rombolà, A. G.; de la Rosa, J. M.; Sakrabani, R.; Sohi, S.; Soja, G.; Valagussa, M.; Verheijen, F.; Zehetner, F., Toward the Standardization of Biochar Analysis: The COST Action TD1107 Interlaboratory Comparison. *Journal of Agricultural and Food Chemistry* **2016,** 64, (2), 513-527.
6. Ippolito, J. A.; Cui, L.; Kammann, C.; Wrage-Mönnig, N.; Estavillo, J. M.; Fuertes-Mendizabal, T.; Cayuela, M. L.; Sigua, G.; Novak, J.; Spokas, K.; Borchard, N., Feedstock choice, pyrolysis temperature and type influence biochar characteristics: a comprehensive meta-data analysis review. *Biochar* **2020,** 2, (4), 421-438.
7. Garcia-Nunez, J. A.; Pelaez-Samaniego, M. R.; Garcia-Perez, M. E.; Fonts, I.; Abrego, J.; Westerhof, R. J. M.; Garcia-Perez, M., Historical Developments of Pyrolysis Reactors: A Review. *Energy & Fuels* **2017,** 31, (6), 5751-5775.
8. Ciesielski, P. N.; Pecha, M. B.; Thornburg, N. E.; Crowley, M. F.; Gao, X.; Oyedeji, O.; Sitaraman, H.; Brunhart-Lupo, N., Bridging Scales in Bioenergy and Catalysis: A Review of Mesoscale Modeling Applications, Methods, and Future Directions. *Energy & Fuels* **2021,** 35, (18), 14382-14400.
9. Vassilev, S. V.; Baxter, D.; Andersen, L. K.; Vassileva, C. G., An overview of the chemical composition of biomass. *Fuel* **2010,** 89, (5), 913-933.
10. Vassilev, S. V.; Baxter, D.; Andersen, L. K.; Vassileva, C. G.; Morgan, T. J., An overview of the organic and inorganic phase composition of biomass. *Fuel* **2012,** 94, 1-33.
11. Patwardhan, P. R.; Satrio, J. A.; Brown, R. C.; Shanks, B. H., Influence of inorganic salts on the primary pyrolysis products of cellulose. *Bioresource Technology* **2010,** 101, (12), 4646-4655.
12. Trendewicz, A.; Evans, R.; Dutta, A.; Sykes, R.; Carpenter, D.; Braun, R., Evaluating the effect of potassium on cellulose pyrolysis reaction kinetics. *Biomass and Bioenergy* **2015,** 74, 15-25.
13. Di Blasi, C.; Galgano, A.; Branca, C., Effects of Potassium Hydroxide Impregnation on Wood Pyrolysis. *Energy & Fuels* **2009,** 23, (2), 1045-1054.
14. Almuina-Villar, H.; Lang, N.; Anca-Couce, A.; Röpcke, J.; Behrendt, F.; Dieguez-Alonso, A., Application of laser-based diagnostics for characterization of the influence of inorganics on the slow pyrolysis of woody biomass. *Journal of Analytical and Applied Pyrolysis* **2019,** 140, 125-136.
15. Paulsen, A. D.; Mettler, M. S.; Dauenhauer, P. J., The Role of Sample Dimension and Temperature in Cellulose Pyrolysis. *Energy & Fuels* **2013,** 27, (4), 2126-2134.
16. Anca-Couce, A., Reaction mechanisms and multi-scale modelling of lignocellulosic biomass pyrolysis. *Progress in Energy and Combustion Science* **2016,** 53, 41-79.
17. Pyle, D. L.; Zaror, C. A., Heat transfer and kinetics in the low temperature pyrolysis of solids. *Chemical Engineering Science* **1984,** 39, (1), 147-158.

18. Maziarka, P.; Anca-Couce, A.; Prins, W.; Ronsse, F., A meta-analysis of thermo-physical and chemical aspects in CFD modelling of pyrolysis of a single wood particle in the thermally thick regime. *Chemical Engineering Journal* **2022,** 446, 137088.
19. Gentile, G.; Debiagi, P. E. A.; Cuoci, A.; Frassoldati, A.; Ranzi, E.; Faravelli, T., A computational framework for the pyrolysis of anisotropic biomass particles. *Chemical Engineering Journal* **2017,** 321, 458-473.
20. Lu, H.; Robert, W.; Peirce, G.; Ripa, B.; Baxter, L. L., Comprehensive Study of Biomass Particle Combustion. *Energy & Fuels* **2008,** 22, (4), 2826-2839.
21. Park, W. C.; Atreya, A.; Baum, H. R., Experimental and theoretical investigation of heat and mass transfer processes during wood pyrolysis. *Combustion and Flame* **2010,** 157, (3), 481-494.
22. Atreya, A.; Olszewski, P.; Chen, Y.; Baum, H. R., The effect of size, shape and pyrolysis conditions on the thermal decomposition of wood particles and firebrands. *International Journal of Heat and Mass Transfer* **2017,** 107, 319-328.
23. Bennadji, H.; Smith, K.; Shabangu, S.; Fisher, E. M., Low-Temperature Pyrolysis of Woody Biomass in the Thermally Thick Regime. *Energy & Fuels* **2013,** 27, (3), 1453-1459.
24. Bennadji, H.; Smith, K.; Serapiglia, M. J.; Fisher, E. M., Effect of Particle Size on Low-Temperature Pyrolysis of Woody Biomass. *Energy & Fuels* **2014,** 28, (12), 7527-7537.
25. Wang, K.; Zhang, H.; Chu, S.; Zha, Z., Pyrolysis of single large biomass particle: Simulation and experiments. *Chinese Journal of Chemical Engineering* **2021,** 29, 375-382.
26. Chen, L.; Dupont, C.; Salvador, S.; Boissonnet, G.; Schweich, D., Influence of Particle Size, Reactor Temperature and Gas Phase Reactions on Fast Pyrolysis of Beech Wood. **2010,** 8, (1).
27. Lang, N.; Rupp, C.; Almuina-Villar, H.; Dieguez-Alonso, A.; Behrendt, F.; Röpcke, J., Pyrolysis behavior of thermally thick wood particles: Time-resolved characterization with laser based in-situ diagnostics. *Fuel* **2017,** 210, 371-379.
28. Almuina-Villar, H.; Sommersacher, P.; Retschitzegger, S.; Anca-Couce, A.; Dieguez Alonso, A., Combined Influence of Inorganics and Transport Limitations on the Pyrolytic Behaviour of Woody Biomass. *Chemical Engineering Transactions* **2020,** 80, 73-78.
29. Gauthier, G.; Melkior, T.; Grateau, M.; Thiery, S.; Salvador, S., Pyrolysis of centimetre-scale wood particles: New experimental developments and results. *Journal of Analytical and Applied Pyrolysis* **2013,** 104, 521-530.
30. Anca-Couce, A.; Sommersacher, P.; Scharler, R., Online experiments and modelling with a detailed reaction scheme of single particle biomass pyrolysis. *Journal of Analytical and Applied Pyrolysis* **2017,** 127, 411-425.
31. Dufour, A.; Girods, P.; Masson, E.; Rogaume, Y.; Zoulalian, A., Synthesis gas production by biomass pyrolysis: Effect of reactor temperature on product distribution. *International Journal of Hydrogen Energy* **2009,** 34, (4), 1726-1734.
32. Mullery, A. A.; Hoang, J. N.; Nguyen, A. T.; Luong, C. D.; Ledesma, E. B., Thermal decomposition pathways of 4-ethylguaiacol under fast pyrolysis and gasification conditions. *Journal of Analytical and Applied Pyrolysis* **2017,** 123, 83-91.
33. Ledesma, E. B.; Hoang, J. N.; Solon, A. J.; Tran, M. M. H.; Nguyen, M. P.; Nguyen, H. D.; Hendrix-Doucette, T.; Vu, J. V.; Fortune, C. K.; Batamo, S., Vapor-Phase Cracking of 4-Vinylguaiacol in a Laminar-Flow Reactor: Kinetics and Effect of Temperature on Product Composition. *Industrial & Engineering Chemistry Research* **2014,** 53, (31), 12527-12536.

34. Norinaga, K.; Shoji, T.; Kudo, S.; Hayashi, J.-i., Detailed chemical kinetic modelling of vapour-phase cracking of multi-component molecular mixtures derived from the fast pyrolysis of cellulose. *Fuel* **2013,** 103, 141-150.

35. Hoekstra, E.; Westerhof, R. J. M.; Brilman, W.; Van Swaaij, W. P. M.; Kersten, S. R. A.; Hogendoorn, K. J. A.; Windt, M., Heterogeneous and homogeneous reactions of pyrolysis vapors from pine wood. *AIChE Journal* **2012,** 58, (9), 2830-2842.

36. Johansson, K. O.; Head-Gordon, M. P.; Schrader, P. E.; Wilson, K. R.; Michelsen, H. A., Resonance-stabilized hydrocarbon-radical chain reactions may explain soot inception and growth. *Science* **2018,** 361, (6406), 997-1000.

37. Ranzi, E.; Debiagi, P. E. A.; Frassoldati, A., Mathematical Modeling of Fast Biomass Pyrolysis and Bio-Oil Formation. Note II: Secondary Gas-Phase Reactions and Bio-Oil Formation. *ACS Sustainable Chemistry & Engineering* **2017,** 5, (4), 2882-2896.

38. Brackmann, C.; Aldén, M.; Bengtsson, P.-E.; Davidsson, K. O.; Pettersson, J. B. C., Optical and Mass Spectrometric Study of the Pyrolysis Gas of Wood Particles. *Applied Spectroscopy* **2003,** 57, (2), 216-222.

39. Ciesielski, P. N.; Crowley, M. F.; Nimlos, M. R.; Sanders, A. W.; Wiggins, G. M.; Robichaud, D.; Donohoe, B. S.; Foust, T. D., Biomass Particle Models with Realistic Morphology and Resolved Microstructure for Simulations of Intraparticle Transport Phenomena. *Energy & Fuels* **2015,** 29, (1), 242-254.

40. Westerhof, R. J. M.; Nygård, H. S.; van Swaaij, W. P. M.; Kersten, S. R. A.; Brilman, D. W. F., Effect of Particle Geometry and Microstructure on Fast Pyrolysis of Beech Wood. *Energy & Fuels* **2012,** 26, (4), 2274-2280.

41. Okekunle, P. O.; Watanabe, H.; Pattanotai, T.; Okazaki, K., Effect of Biomass Size and Aspect Ratio on Intra-Particle Tar Decomposition during Wood Cylinder Pyrolysis. *Journal of Thermal Science and Technology* **2012,** 7, (1), 1-15.

42. Maziarka, P.; Wurzer, C.; Arauzo, P. J.; Dieguez-Alonso, A.; Mašek, O.; Ronsse, F., Do you BET on routine? The reliability of N2 physisorption for the quantitative assessment of biochar's surface area. *Chemical Engineering Journal* **2021,** 418, 129234.

43. Forest Products, L., Wood handbook : wood as an engineering material. In 2021 edition ed.; Forest Products Laboratory, Department of Agriculture of Forest Service Madison, Wisconsin: Madison, Wisconsin, 2021.

44. Plötze, M.; Niemz, P., Porosity and pore size distribution of different wood types as determined by mercury intrusion porosimetry. *European Journal of Wood and Wood Products* **2011,** 69, (4), 649-657.

45. Pfriem, A.; Zauer, M.; Wagenführ, A., Alteration of the pore structure of spruce (Picea abies (L.) Karst.) and maple (Acer pseudoplatanus L.) due to thermal treatment as determined by helium pycnometry and mercury intrusion porosimetry. **2009,** 63, (1), 94-98.

46. Klose, W.; Schinkel, A., Measurement and modelling of the development of pore size distribution of wood during pyrolysis. *Fuel Processing Technology* **2002,** 77-78, 459-466.

47. Lu, S.; Zong, Y., Pore structure and environmental serves of biochars derived from different feedstocks and pyrolysis conditions. *Environmental Science and Pollution Research* **2018,** 25, (30), 30401-30409.

48. Baltrėnas, P.; Baltrėnaitė, E.; Spudulis, E., Biochar from Pine and Birch Morphology and Pore Structure Change by Treatment in Biofilter. *Water, Air, & Soil Pollution* **2015,** 226, (3), 69.

49. Edeh, I. G.; Masek, O.; Fusseis, F., 4D structural changes and pore network model of biomass during pyrolysis. *Scientific Reports* **2023,** 13, (1), 22863.

50. Crowley, M. F.; Sitaraman, H.; Klinger, J.; Usseglio-Viretta, F.; Thornburg, N. E.; Brunhart-Lupo, N.; Pecha, M. B.; Dooley, J. H.; Xia, Y.; Ciesielski, P. N., Measurement of Transport Properties of Woody Biomass Feedstock Particles Before and After Pyrolysis by Numerical Analysis of X-Ray Tomographic Reconstructions. *Frontiers in Energy Research* **2022,** 10.

51. Haag, V.; Dremel, K.; Zabler, S., Volumetric imaging by micro computed tomography: a suitable tool for wood identification of charcoal. *IAWA Journal* **2022,** 44, (2), 210-224.

52. Maziarka, P.; Sommersacher, P.; Wang, X.; Kienzl, N.; Retschitzegger, S.; Prins, W.; Hedin, N.; Ronsse, F., Tailoring of the pore structures of wood pyrolysis chars for potential use in energy storage applications. *Applied Energy* **2021,** 286, 116431.

53. Sommersacher, P.; Kienzl, N.; Brunner, T.; Obernberger, I., Simultaneous Online Determination of S, Cl, K, Na, Zn, and Pb Release from a Single Particle during Biomass Combustion. Part 1: Experimental Setup–Implementation and Evaluation. *Energy & Fuels* **2015,** 29, (10), 6734-6746.

54. Sommersacher, P.; Kienzl, N.; Brunner, T.; Obernberger, I., Simultaneous Online Determination of S, Cl, K, Na, Zn, and Pb Release from a Single Particle during Biomass Combustion. Part 2: Results from Test Runs with Spruce and Straw Pellets. *Energy & Fuels* **2016,** 30, (4), 3428-3440.

55. Corbetta, M.; Frassoldati, A.; Bennadji, H.; Smith, K.; Serapiglia, M. J.; Gauthier, G.; Melkior, T.; Ranzi, E.; Fisher, E. M., Pyrolysis of Centimeter-Scale Woody Biomass Particles: Kinetic Modeling and Experimental Validation. *Energy & Fuels* **2014,** 28, (6), 3884-3898.

56. Branca, C.; Giudicianni, P.; Di Blasi, C., GC/MS Characterization of Liquids Generated from Low-Temperature Pyrolysis of Wood. *Industrial & Engineering Chemistry Research* **2003,** 42, (14), 3190-3202.

57. Dufour, A.; Girods, P.; Masson, E.; Normand, S.; Rogaume, Y.; Zoulalian, A., Comparison of two methods of measuring wood pyrolysis tar. *Journal of Chromatography A* **2007,** 1164, (1), 240-247.

58. Le Brech, Y.; Jia, L.; Cissé, S.; Mauviel, G.; Brosse, N.; Dufour, A., Mechanisms of biomass pyrolysis studied by combining a fixed bed reactor with advanced gas analysis. *Journal of Analytical and Applied Pyrolysis* **2016,** 117, 334-346.

59. Wang, Z.; Cao, J.; Wang, J., Pyrolytic characteristics of pine wood in a slowly heating and gas sweeping fixed-bed reactor. *Journal of Analytical and Applied Pyrolysis* **2009,** 84, (2), 179-184.

60. Estrada Leon, A.; Ramamurthy, R.; Ghysels, S.; Niazi, S.; Prins, W.; Ronsse, F., Analytical (hydro)pyrolysis of pinewood and wheat straw in chloride molten salts: A route for 2-methyl furan production. *Fuel Processing Technology* **2023,** 250, 107917.

61. Undri, A.; Abou-Zaid, M.; Briens, C.; Berruti, F.; Rosi, L.; Bartoli, M.; Frediani, M.; Frediani, P., A simple procedure for chromatographic analysis of bio-oils from pyrolysis. *Journal of Analytical and Applied Pyrolysis* **2015,** 114, 208-221.

62. Bartoli, M.; Rosi, L.; Frediani, M.; Frediani, P., A Simple Protocol for Quantitative Analysis of Bio-Oils through Gas-Chromatography/Mass Spectrometry. *European Journal of Mass Spectrometry* **2016,** 22, (4), 199-212.

63. Scanlon, J. T.; Willis, D. E., Calculation of Flame Ionization Detector Relative Response Factors Using the Effective Carbon Number Concept. *Journal of Chromatographic Science* **1985,** 23, (8), 333-340.

64. Byrne, C. E.; Nagle, D. C., Carbonized wood monoliths—Characterization. *Carbon* **1997,** 35, (2), 267-273.
65. Byrne, C. E.; Nagle, D. C., Carbonization of wood for advanced materials applications. *Carbon* **1997,** 35, (2), 259-266.
66. Jagiello, J.; Ania, C.; Parra, J. B.; Cook, C., Dual gas analysis of microporous carbons using 2D-NLDFT heterogeneous surface model and combined adsorption data of N2 and CO2. *Carbon* **2015,** 91, 330-337.
67. Jagiello, J.; Kenvin, J.; Celzard, A.; Fierro, V., Enhanced resolution of ultra micropore size determination of biochars and activated carbons by dual gas analysis using N2 and CO2 with 2D-NLDFT adsorption models. *Carbon* **2019,** 144, 206-215.
68. Jagiello, J.; Kenvin, J.; Ania, C. O.; Parra, J. B.; Celzard, A.; Fierro, V., Exploiting the adsorption of simple gases O2 and H2 with minimal quadrupole moments for the dual gas characterization of nanoporous carbons using 2D-NLDFT models. *Carbon* **2020,** 160, 164-175.
69. Jagiello, J.; Kenvin, J.; Olivier, J. P.; Lupini, A. R.; Contescu, C. I., Using a New Finite Slit Pore Model for NLDFT Analysis of Carbon Pore Structure. *Adsorption Science & Technology* **2011,** 29, (8), 769-780.
70. Lowell, S.; Shields, J. E.; Thomas, M. A., *Characterization of porous solids and powders surface area, pore size and density*. Springer: Dordrecht, 2011; p 200 - 204.
71. Rouquerol, J.; Baron, G.; Denoyel, R.; Giesche, H.; Groen, J.; Klobes, P.; Levitz, P.; Neimark, A. V.; Rigby, S.; Skudas, R.; Sing, K.; Thommes, M.; Unger, K., Liquid intrusion and alternative methods for the characterization of macroporous materials (IUPAC Technical Report). *Pure and Applied Chemistry* **2011,** 84, (1), 107-136.
72. Soil Science Society of America, *Glossary of soil science terms*. [Rev.] ed.; Soil Science Society of America: Madison, Wis., 2010; p 1 - 88.
73. Di Blasi, C., Modeling chemical and physical processes of wood and biomass pyrolysis. *Progress in Energy and Combustion Science* **2008,** 34, (1), 47-90.
74. Manyà, J. J., Pyrolysis for Biochar Purposes: A Review to Establish Current Knowledge Gaps and Research Needs. *Environmental Science & Technology* **2012,** 46, (15), 7939-7954.
75. Ronsse, F.; van Hecke, S.; Dickinson, D.; Prins, W., Production and characterization of slow pyrolysis biochar: influence of feedstock type and pyrolysis conditions. *GCB Bioenergy* **2013,** 5, (2), 104-115.
76. Sharifzadeh, M.; Sadeqzadeh, M.; Guo, M.; Borhani, T. N.; Murthy Konda, N. V. S. N.; Garcia, M. C.; Wang, L.; Hallett, J.; Shah, N., The multi-scale challenges of biomass fast pyrolysis and bio-oil upgrading: Review of the state of art and future research directions. *Progress in Energy and Combustion Science* **2019,** 71, 1-80.
77. Neves, D.; Thunman, H.; Matos, A.; Tarelho, L.; Gómez-Barea, A., Characterization and prediction of biomass pyrolysis products. *Progress in Energy and Combustion Science* **2011,** 37, (5), 611-630.
78. Anca-Couce, A.; Scharler, R., Modelling heat of reaction in biomass pyrolysis with detailed reaction schemes. *Fuel* **2017,** 206, 572-579.
79. Di Blasi, C.; Branca, C.; Masotta, F.; De Biase, E., Experimental Analysis of Reaction Heat Effects during Beech Wood Pyrolysis. *Energy & Fuels* **2013,** 27, (5), 2665-2674.
80. Di Blasi, C.; Branca, C.; Santoro, A.; Gonzalez Hernandez, E., Pyrolytic behavior and products of some wood varieties. *Combustion and Flame* **2001,** 124, (1), 165-177.

81. Manyà, J. J.; Ruiz, J.; Arauzo, J., Some Peculiarities of Conventional Pyrolysis of Several Agricultural Residues in a Packed Bed Reactor. *Industrial & Engineering Chemistry Research* **2007,** 46, (26), 9061-9070.

82. Di Blasi, C.; Branca, C.; Sarnataro, F. E.; Gallo, A., Thermal Runaway in the Pyrolysis of Some Lignocellulosic Biomasses. *Energy & Fuels* **2014,** 28, (4), 2684-2696.

83. Strezov, V.; Moghtaderi, B.; Lucas, J. A., Computational calorimetric investigation of the reactions during thermal conversion of wood biomass. *Biomass and Bioenergy* **2004,** 27, (5), 459-465.

84. Çengel, Y. A.; Ghajar, A. J.; Kanoglu, M., *Heat and mass transfer: Fundamentals and Applications*. 5th ed.; McGraw-Hill Education: New York, USA, 2014; p 424 - 472.

85. Holman, J. P., *Heat transfer*. 10th ed.; McGraw-Hill: Boston, USA, 2009; p 231 - 242.

86. Lee, C. K.; Chaiken, R. F.; Singer, J. M., Charring pyrolysis of wood in fires by laser simulation. *Symposium (International) on Combustion* **1977,** 16, (1), 1459-1470.

87. Mamleev, V.; Bourbigot, S.; Le Bras, M.; Yvon, J., The facts and hypotheses relating to the phenomenological model of cellulose pyrolysis: Interdependence of the steps. *Journal of Analytical and Applied Pyrolysis* **2009,** 84, (1), 1-17.

88. Wang, X.; Kersten, S. R. A.; Prins, W.; van Swaaij, W. P. M., Biomass Pyrolysis in a Fluidized Bed Reactor. Part 2: Experimental Validation of Model Results. *Industrial & Engineering Chemistry Research* **2005,** 44, (23), 8786-8795.

89. Kwon, T.-W.; Kim, S. D.; Fung, D. P. C., Reaction kinetics of char—CO2 gasification. *Fuel* **1988,** 67, (4), 530-535.

90. Kwon, E. E.; Jeon, E.-C.; Castaldi, M. J.; Jeon, Y. J., Effect of Carbon Dioxide on the Thermal Degradation of Lignocellulosic Biomass. *Environmental Science & Technology* **2013,** 47, (18), 10541-10547.

91. Kwon, E. E.; Cho, S.-H.; Kim, S., Synergetic Sustainability Enhancement via Utilization of Carbon Dioxide as Carbon Neutral Chemical Feedstock in the Thermo-Chemical Processing of Biomass. *Environmental Science & Technology* **2015,** 49, (8), 5028-5034.

92. Wang, L.; Maziarka, P.; Skreiberg, Ø.; Løvås, T.; Wądrzyk, M.; Sevault, A., Study of CO2 gasification reactivity of biocarbon produced at different conditions. *Energy Procedia* **2017,** 142, 991-996.

93. Liaw, S.-S.; Wang, Z.; Ndegwa, P.; Frear, C.; Ha, S.; Li, C.-Z.; Garcia-Perez, M., Effect of pyrolysis temperature on the yield and properties of bio-oils obtained from the auger pyrolysis of Douglas Fir wood. *Journal of Analytical and Applied Pyrolysis* **2012,** 93, 52-62.

94. Yogalakshmi, K. N.; Poornima Devi, T.; Sivashanmugam, P.; Kavitha, S.; Yukesh Kannah, R.; Varjani, S.; Adish Kumar, S.; Kumar, G.; Rajesh Banu, J., Lignocellulosic biomass-based pyrolysis: A comprehensive review. *Chemosphere* **2022,** 286, 131824.

95. Fuentes-Cano, D.; Gómez-Barea, A.; Nilsson, S.; Ollero, P., Kinetic Modeling of Tar and Light Hydrocarbons during the Thermal Conversion of Biomass. *Energy & Fuels* **2016,** 30, (1), 377-385.

96. Williams, P. T.; Besler, S., The influence of temperature and heating rate on the slow pyrolysis of biomass. *Renewable Energy* **1996,** 7, (3), 233-250.

97. Choi, Y. S.; Johnston, P. A.; Brown, R. C.; Shanks, B. H.; Lee, K.-H., Detailed characterization of red oak-derived pyrolysis oil: Integrated use of GC, HPLC, IC, GPC and Karl-Fischer. *Journal of Analytical and Applied Pyrolysis* **2014,** 110, 147-154.

98. Staš, M.; Auersvald, M.; Kejla, L.; Vrtiška, D.; Kroufek, J.; Kubička, D., Quantitative analysis of pyrolysis bio-oils: A review. *TrAC Trends in Analytical Chemistry* **2020,** 126, 115857.

99. Ferrell III, J. R.; Olarte, M. V.; Christensen, E. D.; Padmaperuma, A. B.; Connatser, R. M.; Stankovikj, F.; Meier, D.; Paasikallio, V., Standardization of chemical analytical techniques for pyrolysis bio-oil: history, challenges, and current status of methods. *Biofuels, Bioproducts and Biorefining* **2016,** 10, (5), 496-507.

100. Stankovikj, F.; McDonald, A. G.; Helms, G. L.; Garcia-Perez, M., Quantification of Bio-Oil Functional Groups and Evidences of the Presence of Pyrolytic Humins. *Energy & Fuels* **2016,** 30, (8), 6505-6524.

101. Brewer, C. E.; Chuang, V. J.; Masiello, C. A.; Gonnermann, H.; Gao, X.; Dugan, B.; Driver, L. E.; Panzacchi, P.; Zygourakis, K.; Davies, C. A., New approaches to measuring biochar density and porosity. *Biomass and Bioenergy* **2014,** 66, 176-185.

102. Wood, R.; Masek, O.; Erastova, V., *Biochars at the molecular level. Part 1 -- Insights into the molecular structures within biochars*. 2023.

103. Li, F.; Wu, K.; Yang, K.; Ge, Z.; Feng, J.; Zhang, H., A comprehensive pyrolysis model for lignocellulosic biomass particles with a special emphasis on the anisotropic characteristics. *Fuel* **2023,** 341, 127635.

104. Hastaoglu, M. A.; Berruti, F., A gas-solid reaction model for flash wood pyrolysis. *Fuel* **1989,** 68, (11), 1408-1415.

105. Moore, G. R.; Blankenhorn, P. R.; Beall, F. C.; Kline, D. E., Some Physical Properties of Birch Carbonized in A Nitrogen Atmosphere. *Wood and Fiber Science* **1974,** 6, 193-199.

106. Davidsson, K. O.; Pettersson, J. B. C., Birch wood particle shrinkage during rapid pyrolysis. *Fuel* **2002,** 81, (3), 263-270.

107. Caposciutti, G.; Almuina-Villar, H.; Dieguez-Alonso, A.; Gruber, T.; Kelz, J.; Desideri, U.; Hochenauer, C.; Scharler, R.; Anca-Couce, A., Experimental investigation on biomass shrinking and swelling behaviour: Particles pyrolysis and wood logs combustion. *Biomass and Bioenergy* **2019,** 123, 1-13.

108. Huang, Q. X.; Wang, R. P.; Li, W. J.; Tang, Y. J.; Chi, Y.; Yan, J. H., Modeling and Experimental Studies of the Effects of Volume Shrinkage on the Pyrolysis of Waste Wood Sphere. *Energy & Fuels* **2014,** 28, (10), 6398-6406.

109. M. Kumar, B. B. V. R. C. G., Mechanical Properties of Acacia and Eucalyptus Wood Chars. *Energy Sources* **1999,** 21, (8), 675-685.

110. Kumar, M.; Jena, S., Influence of Carbonization Conditions on the Properties of Coconut Shell Chars. *Energy Sources, Part A: Recovery, Utilization, and Environmental Effects* **2006,** 28, (5), 423-431.

111. Zickler, G. A.; Schöberl, T.; Paris, O., Mechanical properties of pyrolysed wood: a nanoindentation study. *Philosophical Magazine* **2006,** 86, (10), 1373-1386.

112. Zickler, G. A.; Wagermaier, W.; Funari, S. S.; Burghammer, M.; Paris, O., In situ X-ray diffraction investigation of thermal decomposition of wood cellulose. *Journal of Analytical and Applied Pyrolysis* **2007,** 80, (1), 134-140.

113. Yoo, S.; Kelley, S. S.; Tilotta, D. C.; Park, S., Structural Characterization of Loblolly Pine Derived Biochar by X-ray Diffraction and Electron Energy Loss Spectroscopy. *ACS Sustainable Chemistry & Engineering* **2018,** 6, (2), 2621-2629.

114. McDonald-Wharry, J. S.; Manley-Harris, M.; Pickering, K. L., Reviewing, Combining, and Updating the Models for the Nanostructure of Non-Graphitizing Carbons Produced from Oxygen-Containing Precursors. *Energy & Fuels* **2016,** 30, (10), 7811-7826.
115. De Smedt, J.; Heynderickx, P. M.; Arauzo, P. J.; Ronsse, F., Adsorption mechanism of different dyes on chemical activated carbon as quantitative assessment for wastewater treatment: Comparative study between ZnCl2 and its eutectic. *Separation and Purification Technology* **2024,** 334, 126002.
116. Hass, P.; Wittel, F. K.; McDonald, S. A.; Marone, F.; Stampanoni, M.; Herrmann, H. J.; Niemz, P., Pore space analysis of beech wood: The vessel network. **2010,** 64, (5), 639-644.
117. Niemz, P.; Teischinger, A.; Sandberg, D., Springer handbook of wood science and technology. In Springer Cham: Cham, 2023; pp 35-137, 178-279, 280-353, 354-297.
118. DIN EN 1860-2. In *Appliances, solid fuels and firelighters for barbecuing - Part 2: Barbecue charcoal and barbecue charcoal briquettes - Requirements and test methods*.
119. Food Agriculture Organization of the United Nations - Mechanical Wood Products Branch, *Industrial charcoal making*. FAO United Nations Rome: Rome, 1985; p 1 - 133.
120. Henning, K.-D.; von Kienle, H., Activated Carbon. In *Industrial Carbon and Graphite Materials*, Wiley-VCH: Weinheim, DE, 2021; Vol. I, pp 491-531.
121. Wachtler, M.; Öttinger, O.; Schweiss, R., Carbon and Graphite for Electrochemical Power Sources. In *Industrial Carbon and Graphite Materials*, Wiley-VCH: Weinheim, DE, 2021; Vol. I, pp 379-455.
122. De Smedt, J.; Arauzo, P. J.; Maziarka, P.; Ronsse, F., Adsorptive carbons from pinewood activated with a eutectic mixture of molten chloride salts: Influence of temperature and salt to biomass ratio. *Journal of Cleaner Production* **2022,** 376, 134216.
123. Aguiar, J. E.; de Oliveira, J. C. A.; Silvino, P. F. G.; Neto, J. A.; Silva, I. J.; Lucena, S. M. P., Correlation between PSD and adsorption of anionic dyes with different molecular weigths on activated carbon. *Colloids and Surfaces A: Physicochemical and Engineering Aspects* **2016,** 496, 125-131.
124. Duarte, E. D. V.; Oliveira, M. G.; Spaolonzi, M. P.; Costa, H. P. S.; Silva, T. L. d.; Silva, M. G. C. d.; Vieira, M. G. A., Adsorption of pharmaceutical products from aqueous solutions on functionalized carbon nanotubes by conventional and green methods: A critical review. *Journal of Cleaner Production* **2022,** 372, 133743.
125. Bernal, V.; Giraldo, L.; Moreno-Piraján, J. C., Adsorption of Pharmaceutical Aromatic Pollutants on Heat-Treated Activated Carbons: Effect of Carbonaceous Structure and the Adsorbent–Adsorbate Interactions. *ACS Omega* **2020,** 5, (25), 15247-15256.
126. Buiel, E. R.; George, A. E.; Dahn, J. R., Model of micropore closure in hard carbon prepared from sucrose. *Carbon* **1999,** 37, (9), 1399-1407.
127. Wiener, M.; Reichenauer, G., Microstructure of porous carbons derived from phenolic resin – Impact of annealing at temperatures up to 2000°C analyzed by complementary characterization methods. *Microporous and Mesoporous Materials* **2015,** 203, 116-122.
128. International Biochar Initiative (IBI), Standardized Product Definition and Product Testing Guidelines for Biochar that Is Used in Soil, IBI-STD-2.1, 2015. In.
129. European Biochar Foundation (EBC), European Biochar Certificate - Guidelines for a Sustainable Production of Biochar, Version 9.0E, 2020, Arbaz, CH. In.
130. Rathnayake, D.; Maziarka, P.; Ghysels, S.; Mašek, O.; Sohi, S.; Ronsse, F., How to trace back an unknown production temperature of biochar from chemical characterization methods in a feedstock independent way. *Journal of Analytical and Applied Pyrolysis* **2020,** 151, 104926.

131. Buss, W.; Graham, M. C.; MacKinnon, G.; Mašek, O., Strategies for producing biochars with minimum PAH contamination. *Journal of Analytical and Applied Pyrolysis* **2016,** 119, 24-30.
132. Buss, W.; Hilber, I.; Graham, M. C.; Mašek, O., Composition of PAHs in Biochar and Implications for Biochar Production. *ACS Sustainable Chemistry & Engineering* **2022,** 10, (20), 6755-6765.
133. Edeh, I. G.; Mašek, O.; Buss, W., A meta-analysis on biochar's effects on soil water properties – New insights and future research challenges. *Science of The Total Environment* **2020,** 714, 136857.
134. Adhikari, S.; Timms, W.; Mahmud, M. A. P., Optimising water holding capacity and hydrophobicity of biochar for soil amendment – A review. *Science of The Total Environment* **2022,** 851, 158043.
135. Bunk, B.; Schulz, A.; Stammen, S.; Münch, R.; Warren, M. J.; Jahn, D.; Biedendieck, R., A short story about a big magic bug. *Bioengineered Bugs* **2010,** 1, (2), 85-91.